Applied Mathematical Modelling 158 (2026) 117007

Contents lists available at ScienceDirect

Applied Mathematical Modelling

journal homepage: www.elsevier.com/locate/apm

Interaction of a circular porous cylinder with an unconfined steady flow at the *mesoscopic* scale

Costanza Aricò [a,*], Rainer Helmig [b], Martin Schneider [b]

[a] Department of Engineering, University of Palermo, viale delle Scienze, Palermo, 90128, Italy
[b] Institute for Modelling Hydraulic and Environmental Systems (IWS), Department of Hydromechanics and Modelling of Hydrosystems, University of Stuttgart, Pfaffenwaldring 61, Stuttgart, D-70569, Germany

ARTICLE INFO

Keywords:
Free fluid-porous medium interaction
Wake past a cylinder
One-domain-approach
Averaging techniques
Mesoscopic scale
REV-size effects

ABSTRACT

We investigate the interaction of a circular porous cylinder with a steady unconfined flow based on a mesoscopic One-Domain Approach (ODA) at the Representative Elementary Volume (REV) scale. Unlike classical penalized methods, which impose sharp discontinuities at the fluid-porous interface, our method resolves the transition zone explicitly, using space-dependent porosity and permeability profiles extracted from filtered pore-scale simulations (PSSs). A curvilinear permeability framework is introduced, aligning the principal anisotropy directions with the tangential and normal vectors of the cylinder surface, which significantly improves prediction of viscous shear, pressure-driven filtration, and flow penetration. We show that the size and shape of mesoscopic profiles, controlled by the REV, act as a "hydrodynamic buffer" governing momentum transfer, interface penetration, and wake structure. Smaller REVs reproduce reference PSS data accurately, while larger REVs overpredict wake extension and underpredict drag, highlighting the sensitivity of macroscopic forces to the transition zone. Comparisons with conventional penalized models reveal systematic overestimation of drag and underestimation of flow penetration, demonstrating the limitations of abrupt-interface approximations. This approach leverages the scalability and data-driven nature of PSS-informed profiles, providing a robust, computationally efficient tool for complex flows. The methodology is particularly relevant for applications where interface-resolved hydrodynamics determine performance. Our results emphasize that explicit treatment of the mesoscopic transition zone is critical to capture realistic drag, wake dynamics, and momentum transfer, offering a generalizable alternative to traditional macroscopic or penalized ODA models.

1. Introduction

The hydrodynamic study of flow past and through porous bodies is of significant interest for numerous industrial, biomedical, and environmental applications, such as flow in fractured media [1], PEM fuel cells [2], passive flow control techniques [3], alloy solidification [4], transvascular flow in biological vessels [5], seed wind dispersion [6], porous scaffolds in tissue engineering, biological and industrial filters, floc settling in liquid-solid reactors, and thermal insulation (e.g., [7–10] and references therein).

Several numerical approaches have been applied to these problems. At the microscopic pore-scale, the porous matrix, composed of solid inclusions (SIs), is explicitly resolved (e.g., [11]). While highly accurate, this approach involves a very high computational cost, due to the wide separation of characteristic length scales between the solid inclusions, l_s, the pores, l_p, and the macroscopic domain size, L (see Fig. 1).

* Corresponding author.
E-mail address: costanza.arico@unipa.it (C. Aricò).

https://doi.org/10.1016/j.apm.2026.117007
Received 31 December 2025; Received in revised form 2 April 2026; Accepted 20 April 2026
Available online 28 April 2026

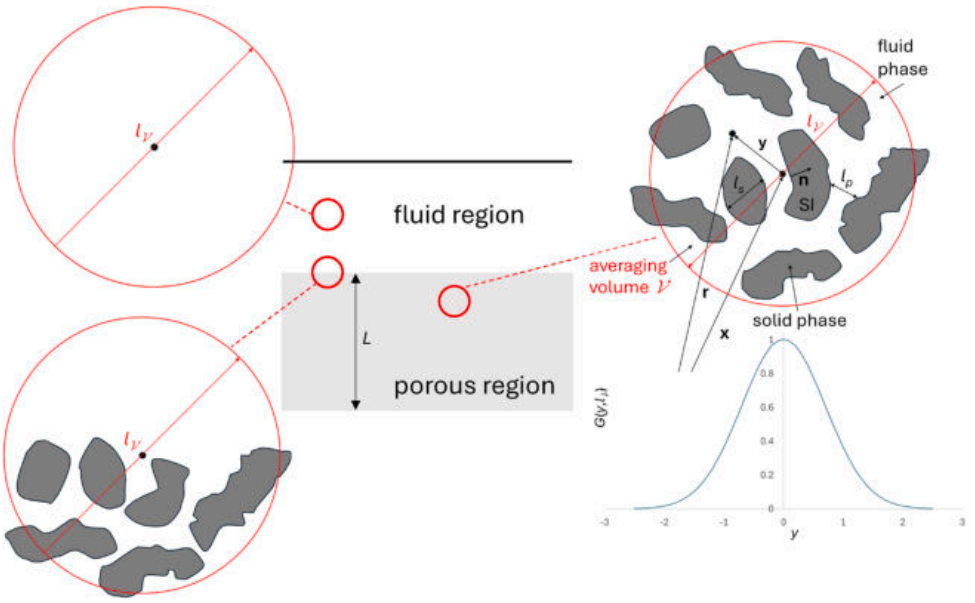

Fig. 1. The volume averaging and the 1D filter function $G(y, l_y)$.

For this reason, averaged-scale approaches have become popular. These continuum upscaled methods describe the porous medium using its effective properties, namely the porosity and the permeability tensor. The most common approaches at this scale are the "Two-Domain Approach" (TDA) and the "One-Domain Approach" (ODA).

In the TDA, two separate sets of governing equations are solved: the (Navier-)Stokes equations in the fluid region and Darcy-type equations in the porous domain, coupled through a sharp interface. Specific boundary conditions must be imposed at the interface (e.g., the Beavers–Joseph conditions [12]). The porous region is described using bulk porosity and permeability coefficients, and the TDA represents a macroscopic level of description (e.g., [13]).

In contrast, the ODA treats the fluid and porous regions as a *single fictitious medium* with spatially varying porosity and permeability coefficients. A single set of governing equations is solved, rigorously derived using the volume-averaging technique. Across the interface, the porosity and permeability vary continuously from their bulk porous values to those of the free fluid (e.g., [13]). This smooth transition defines a "transition layer" of size s_{TL}, such that $l_s < s_{TL} << L$, consistent with [14], who noted that "an interface is an ideal representation of a region with continuous spatial changes of the macroscopic properties, and that knowledge of these evolving heterogeneities is necessary for an accurate description of transport phenomena near the interface." Consequently, the ODA provides a *mesoscopic* level of description (e.g., [13,14]) and eliminates the need for ad hoc interface parameters as in TDA, which could be difficult to define for complex geometries.

A widely used ODA variant is the so-called "penalized" approach. This can be regarded as a macroscopic ODA, where a single set of governing equations is solved across the entire domain, with an additional Darcy-like force term representing the influence of the porous matrix (e.g., [3,9,15–20]). In this approach, porosity and permeability are assumed discontinuous at the interface, activating the force term only in the porous region, typically via Ergun-type equations based on porosity, characteristic solid size l_s, and empirical coefficients. The penalized approach is widely adopted due to its relatively simple integration into existing Navier–Stokes solvers.

In this work, we investigate the interaction of a circular porous cylinder with a steady, unconfined flow. Unlike most previous studies that employ penalized approaches (e.g., [7–9,18,21,22]), we apply a *mesoscopic ODA* where the porosity and permeability profiles in both the bulk and transition layer are derived by applying filtering techniques to preliminary pore-scale simulations (PSSs). This method explicitly resolves the interface without imposing scale separation, and the shape and size of the resulting mesoscopic profiles significantly affect wake dynamics and hydrodynamic forces, highlighting discrepancies with conventional penalized models.

Several studies have derived averaged porosity and permeability profiles from PSSs (e.g., [23–25]), but these typically assume 1D flow parallel to the porous surface, assumed to be aligned with the Cartesian coordinate axes. In contrast, the present study considers a 2D flow around a circular cylinder and aligns the principal directions of the permeability tensor along the tangential and normal directions of the cylinder surface. This strategy improves the physical representation of tangential shear and pressure-driven flow, compared with the conventional alignment along Cartesian axes.

Theoretical approaches based on homogenization (e.g., [26]) are constrained by scale separation and medium periodicity, which limits their accuracy in transition zones with strong gradients. Generalized Transport Equation-based methods (e.g., [27,28]) can predict spatially varying properties but require a unique macroscopic pressure gradient, and periodicity, which complicates their application to irregular flows and geometries. Specifically, the closure problems would need to be redefined for every morphological variation, leading to a level of complexity that often outweighs the practical advantages of these analytical methods. Recent ODA extensions (e.g., [29,30]) have been proposed as "simplified version of the volume averaging method". They incorporate inertial and slip effects and a unified Darcy-like flow equation is proposed in the entire domain, based on a position-dependent apparent

permeability tensor. This tensor is derived by solving closure problems within the bulk- and transition region; however, such a procedure typically relies on the assumptions of local periodicity of the porous microstructure, unique macroscopic pressure gradient, length scale constraints in the transition zone (e.g., Eqs. (15) and (16) in [30]), and require iterative determination of transition-layer size, limiting scalability to complex real-world geometries.

In contrast, our ODA recovers the essential physics of the transition layer by directly informing the local constitutive closure with pore-scale data, thus accounting for non-periodic effects and interface geometry without the need for solving auxiliary theoretical closure problems. By mapping the pore-scale dynamics into spatially-varying, scalable profiles of porosity and permeability, we capture the essential physics of the momentum exchange at the interface. This strategy provides a pragmatic and robust framework that maintains the accuracy of pore-scale insights while ensuring the computational efficiency required for large-scale engineering applications. Specifically, we investigate how the size and shape of the transition zone – through the profiles of porosity and permeability – influence (1) the flow field, with particular attention to wake geometry and hydrodynamic forces, and (2) numerical errors relative to a reference averaged PSSs solution. This study demonstrates the advantages of the mesoscopic approach over volume-averaging and penalized methods, with important implications for practical applications.

Rather than a sharp interface, the fluid-porous transition layer behaves as a “hydrodynamic buffer” that redistributes momentum exchange over a finite region. Its thickness and profile directly regulate the balance between momentum penetration and viscous dissipation, ultimately controlling drag and wake structure.

This perspective provides a physical interpretation of the discrepancies observed in classical penalized approaches.

Outline of the paper. In Section 2, we recall the derivation of mesoscopic governing equations from pore-scale equations. In Section 3, we describe the computation of porosity and permeability profiles in the bulk porous region and the transition layer. In Section 4, we study the interaction of an unconfined flow with a circular porous cylinder, analyzing the effects of computational grid size and the shape of porous medium property profiles at the interface.

2. The averaging operations from the pore to the averaged-scale

In the following, we consider a Newtonian incompressible fluid both around and within a homogeneous, isotropic, and saturated porous medium, whose solid inclusions (SIs) are rigid and fixed in space. At the microscopic pore-scale (see Fig. 1), the flow in the fluid region (i.e., within the void space) is governed by the incompressible Navier–Stokes equations,

$$\frac{\partial \mathbf{u}}{\partial t} + \mathbf{u}\cdot\nabla\mathbf{u} = -\nabla\Psi + \nu\nabla^2\mathbf{u}, \tag{1a}$$

$$\nabla\cdot\mathbf{u} = 0, \tag{1b}$$

where ρ, μ, $\mathbf{u}$, and p denote the fluid density, dynamic viscosity, velocity, and pressure, respectively. Here, $\Psi = p/\rho$ and $\nu = \mu/\rho$, with Ψ commonly referred to as the *kinematic pressure*.

In addition to the external boundaries of the domain, boundary conditions are imposed at the fluid–solid interfaces within the porous medium.

As mentioned in Section 1, we briefly recall how the averaged-scale governing equations are obtained via *volume averaging* of the pore-scale equations Eq. (1). Let $\mathcal{V}$ denote the averaging volume, and define the Representative Elementary Volume (REV) as the portion of the domain contained within $\mathcal{V}$. For disordered porous media, the characteristic length scale $l_{\mathcal{V}}$ (see Fig. 1) is typically assumed to satisfy [31,32]

$$l_p \simeq l_s \ll l_{\mathcal{V}} \ll L, \tag{2}$$

although, as noted by Whitaker [32], this scale separation is not a strict requirement for the applicability of the averaging procedure. For ordered porous structures, Quintard and Whitaker [33] demonstrate that the REV size consistently aligns with the characteristic dimensions of a geometrical unit cell. This choice ensures that the averaged quantities capture the periodic nature of the medium, effectively bridging the gap between volume averaging and classical homogenization theory [26].

Given any microscopic (scalar or vector) quantity Φ, its *surface average* $\langle\Phi\rangle_{\mathbf{x}}$ and *intrinsic average* $\langle\Phi\rangle^i_{\mathbf{x}}$, evaluated at the centroid $\mathbf{x}$ of $\mathcal{V}$, are defined as (e.g., [31,32])

$$\langle\Phi\rangle_{\mathbf{x}} = \int_{\mathcal{V}} G(\mathbf{y}, l_{\mathcal{V}})\gamma(\mathbf{r})\Phi(\mathbf{r})\, dV, \qquad \langle\Phi\rangle^i_{\mathbf{x}} = \frac{\langle\Phi\rangle_{\mathbf{x}}}{\phi_{\mathbf{x}}},$$

where $\mathbf{y} = \mathbf{r} - \mathbf{x}$, $G(\mathbf{y}, l_{\mathcal{V}})$ is a filtering (weighting) function with characteristic size $l_{\mathcal{V}}$, and $\gamma(\mathbf{r})$ is the phase indicator function, equal to 1 in the fluid phase and 0 otherwise. The porosity at $\mathbf{x}$ is defined as

$$\phi_{\mathbf{x}} = \int_{\mathcal{V}} G(\mathbf{y}, l_{\mathcal{V}})\gamma(\mathbf{r})\, dV. \tag{3}$$

The filter function must satisfy the normalization condition

$$\int_{\mathcal{V}} G(\mathbf{y}, l_{\mathcal{V}})\, dV = 1,$$

and possess compact support (e.g., [33]). The resulting averaged fields are continuous across phases, provided that $l_{\mathcal{V}}$ is sufficiently large. For notational simplicity, the subscript $\mathbf{x}$ will be omitted hereafter.

Applying the volume averaging procedure to Eq. (1) yields the REV-scale governing equations (e.g., [4,13,14])

$$\nabla \cdot \langle \mathbf{u} \rangle = 0, \tag{4a}$$

$$\frac{\partial \langle \mathbf{u} \rangle}{\partial t} + \langle \mathbf{u} \rangle \cdot \nabla \left(\frac{\langle \mathbf{u} \rangle}{\phi} \right) = -\phi \nabla \langle \Psi \rangle^i + \nu \nabla^2 \langle \mathbf{u} \rangle + \mathbf{F}_d, \tag{4b}$$

where t denotes time, $\langle \mathbf{u} \rangle$ is the superficial average velocity, $\langle \Psi \rangle^i = \langle p \rangle^i / \rho$, and $\mathbf{F}_d$ represents the force exerted by the SIs on the fluid. The superficial velocity is typically preferred because it is solenoidal, whereas the intrinsic pressure is closer to experimentally measured quantities [13,34].

The term $\mathbf{F}_d$ is rigorously obtained from the averaging procedure and reads (e.g., [13,23,25,32,35,36])

$$\mathbf{F}_d = -\langle \Psi \rangle^i \nabla \phi - \int_S [G(-\Psi \mathbf{I} + \nu \nabla \mathbf{u}) \cdot \mathbf{n}] ds, \tag{5}$$

where S denotes the fluid–solid interface within the REV and $\mathbf{n}$ is the unit normal pointing into the solid phase (see Fig. 1). Notably, no scale separation assumption as in Eq. 2 is required for this expression (see also Eqs. (B.1), (B.2) in Appendix B).

Other formulations of $\mathbf{F}_d$ have been derived in the literature under the scale constraint $l_\mathcal{V} \ll L$, where the deviations of the instantaneous values of Ψ and $\mathbf{u}$ from their intrinsic averages appear in the surface integral on the right-hand side of Eq. (5) (e.g., [28]). In such formulations, an additional correction term arises in the momentum equation (the so-called "second Brinkman term"), proportional to the gradients of porosity and intrinsic velocity. The scale constraint $l_\mathcal{V} \ll L$ may not hold in the transition zone due to the rapid spatial variation of macroscopic flow variables across the interface (see Eqs. (B.5) to (B.7) in Appendix B).

The term $\mathbf{F}_d$ in Eq. (5) requires closure, as it depends on the unknown pore-scale fields Ψ and $\mathbf{u}$.

While deriving Eq. (4) and adopting the closure for $\mathbf{F}_d$, the inertial effects at the pore-scale are assumed negligible. This assumption is consistent with the conditions of the present study, as demonstrated in the following sections. Physically, this corresponds to low-permeability media, where the fluid velocity within the porous region is significantly smaller than in the free-fluid region (e.g., [36]). Momentum exchange between fluid layers is strongly hindered by the dense solid matrix, resulting in negligible convective effects. Under these conditions, both the subfilter-scale stress term (e.g., [37]) and the Forchheimer correction (e.g., [38]) are neglected in Eq. (4b). The term $\langle \mathbf{u} \rangle \cdot \nabla(\langle \mathbf{u} \rangle / \phi)$ is retained in Eq. (4b) to account for the fluid dynamics in the free-stream and wake regions.

Following the theoretical framework proposed in [13,39], we assume that the forces acting within the transition zone are of the same nature as those in the bulk porous region (e.g., [7,13,32–34]). This modeling choice represents the heterogeneous transition layer through spatial variations of porosity and permeability. Accordingly, the closure of $\mathbf{F}_d$ is

$$\mathbf{F}_d = \nu \phi(\mathbf{x}) \mathfrak{K}(\mathbf{x}) \langle \mathbf{u} \rangle, \tag{6}$$

where $\mathbf{x}$ is the position vector within the transition zone and $\mathfrak{K}$ in the inverse of the permeability tensor $\mathbf{K}$, symmetric and positive definite. Eq. (6) defines a mesoscopic drag force in which the spatial heterogeneity of the porous structure is encapsulated in the fields $\phi(\mathbf{x})$ and $\mathfrak{K}(\mathbf{x})$, derived directly from pore-scale data (see Section 3.2). The pore-scale Reynolds numbers further support the assumption of negligible inertial effects, even within the transition region (see Section 3.1).

It should be noted that, from a formal upscaling perspective (e.g., Volume Averaging Theory), a mathematically exact one-domain description of the interface requires the inclusion of non-local closure terms to account for the breakdown of scale separation [30,34]. However, solving such non-local closure problems on curvilinear and finite-size manifolds remains a challenge. Recent one-domain models [29,30] rely on a simplified version of the Volume Averaging Theory, using an apparent permeability tensor, which is derived by assuming local periodicity and scale separation even within the transition zone. However, these assumptions may not fully capture the physics at the interface, especially when dealing with curved geometries or finite-sized domains. In the present ODA, we adopt a local constitutive closure, but it is directly informed by PSSs, which is based on spatially-varying effective properties $\phi(\mathbf{x})$ and $\mathfrak{K}(\mathbf{x})$. It serves as a high-fidelity local closure that incorporates pore-scale physics directly, providing a pragmatic and computationally efficient framework for complex geometries.

In the following sections, ϕ_0 and $\mathfrak{K}_0$ denote the porosity and inverse permeability tensor in the bulk porous region.

3. Calculation of the porosity and permeability at the averaged-scale

In this section, we describe the methodology adopted to compute the macroscopic properties of the porous medium, i.e., the porosity and the coefficients of the permeability tensor. PSSs are performed (see Section 3.1), and the resulting velocity and pressure fields are subsequently averaged using filtering operations (see Section 3.2). These are used to evaluate the term $\mathbf{F}_d$ in Eq. (5) and to determine the coefficients of the permeability tensor via Eq. (6). The porosity within both the bulk porous region and the transition zone is obtained from Eq. (3).

3.1. Pore-scale simulations (PSSs)

We performed a set of PSSs considering a porous cylinder immersed in an unconfined uniform flow, according to the setup shown in Fig. 2, top row. The porous material is assumed homogeneous and isotropic, composed of unit cells, each containing a centrally located circular SI (see Fig. 2, bottom row). No-slip boundary conditions are imposed at the fluid–solid interfaces within the porous cylinder.

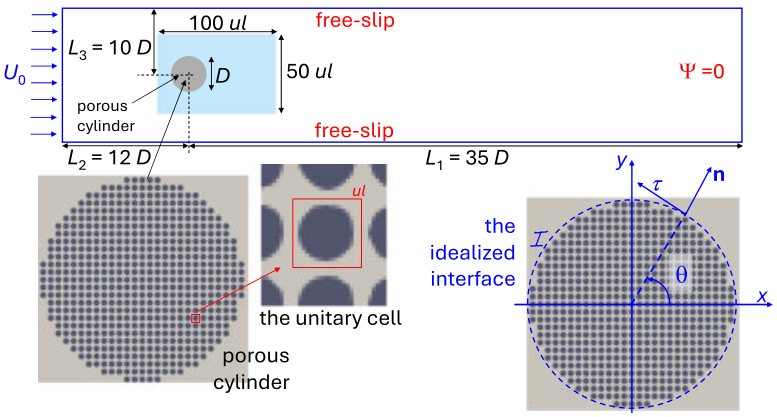

Fig. 2. Top row : setup and BCs of the PSSs. The PSSs results were filtered in the cyan area. Bottom left, the homogeneous porous cylinder made of unitary cells *ul*, bottom right, the "idealized" interface $\mathcal{I}$ with its normal and tangential unit vectors **n** and $\boldsymbol{\tau}$.

Table 1
Number of triangles and vertices of the grids used for the PSSs.

Material	ϕ_0	# parts for SI boundary discretization	N_T	N_V
M1	0.4	$\simeq 152$	2,089,825	1,091,979
M2	0.5	$\simeq 140$	1,906,569	980,335
M3	0.65	$\simeq 116$	2,095,896	1,083,998

The diameter of the porous cylinder is $D = 27ul$. The size of the unit cell is $ul = 5 \cdot 10^{-04}$ m. By varying the SI diameter, d_{SI}, three porous materials are considered, with bulk porosity $\phi_0 = (V_{cell} - V_{SI})/V_{cell}$, equal to 0.4, 0.5, and 0.65, respectively. Here, V_{cell} and V_{SI} denote the volumes (areas in 2D) of the unit cell and the SI. In the following, these materials are referred to as "material 1" (M1), "material 2" (M2), and "material 3" (M3), respectively.

We set $\nu = 1 \cdot 10^{-06}\ \frac{\mathrm{m}^2}{\mathrm{s}}$ and prescribe an undisturbed velocity $\mathbf{U}_0 = \left(U_{0,x}, U_{0,y}\right)^T$, with $U_{0,y} = 0$ and $2 \cdot 10^{-04} \leq U_{0,x} \leq 1 \cdot 10^{-02}$ m/s. The (macroscopic) Reynolds number, $Re = \frac{U_{0,x} D}{\nu}$, ranges from approximately 2.7 to 130, while the pore-scale Reynolds number, $Re_p = \frac{\langle \mathbf{u} \rangle d_{SI}}{\nu}$, lies in the range $1 \cdot 10^{-04} \leq Re_p \leq 9.7 \cdot 10^{-02}$, including the regions near the fluid–porous interface. This further supports the assumption of negligible inertial effects within the porous medium (see Section 2). The choice of the computational domain size is discussed in Section 3.2.

The PSSs were carried out using the in-house numerical solver recently presented and validated in [40–42]. The computational domain was discretized using unstructured, body-fitted triangular meshes. The algorithm employs a fractional-step procedure at each time iteration, consisting of a predictor and two corrector steps. A marching-in-space-and-time procedure is adopted for the predictor problem, which provides significant advantages in handling the nonlinear convective terms in the momentum equations (see the cited references). The two corrector steps require the solution of large linear systems with sparse, symmetric, and positive definite matrices satisfying the M-matrix property on unstructured Delaunay grids. An efficient solution is obtained using a preconditioned conjugate gradient method with incomplete Cholesky factorization. The velocity field at each time step belongs to the RT_0 space within each simplex of the mesh, while the pressure is piecewise linear. The scheme ensures a pointwise divergence-free velocity field and flux continuity across element interfaces. Further details can be found in [40–42].

In Fig. 2, top row, the imposed boundary conditions are shown: an undisturbed velocity $\mathbf{U}_0$ at the inlet, zero pressure at the outlet, and free-slip conditions (see [40–42]) at the upper and lower boundaries of the domain, in addition to the no-slip conditions at the SI surfaces.

The grid size h used in the PSSs ranges from approximately $h \simeq 0.018ul$ within the porous medium and in the fluid region near the cylinder, to $h \simeq 2.5ul$ in the far-field region. This ensures a fine resolution within the porous structure; in particular, each SI boundary is discretized using the number of segments reported in Table 1. The same table also lists the total number of grid elements N_T and vertices N_V. A convergence study has been performed to determine a suitable grid size within the porous medium. This region was initially discretized using three different grid resolutions: "coarse" ($h \simeq 0.027ul$), "medium" ($h \simeq 0.018ul$), and "fine" ($h \simeq 0.012ul$). The grid size in the far-field region was kept unchanged. At the end of Section 3.2 (see also Table 4), we show that the relative difference in the permeability coefficients obtained using the "medium" and "fine" grids is approximately 1%. This indicates that the selected grid size provides a good compromise between computational cost and accuracy, with negligible differences compared to finer discretizations.

3.2. Filtering operations

Several filtering functions $G(\mathbf{y}, l_y)$ have been proposed in the literature, e.g., the "cellular" (or triangular), "quartic", "top-hat" (or constant), and "Gaussian" filters (e.g., [25,33]). To strictly satisfy the requirement of compact support (see Section 2), we employed

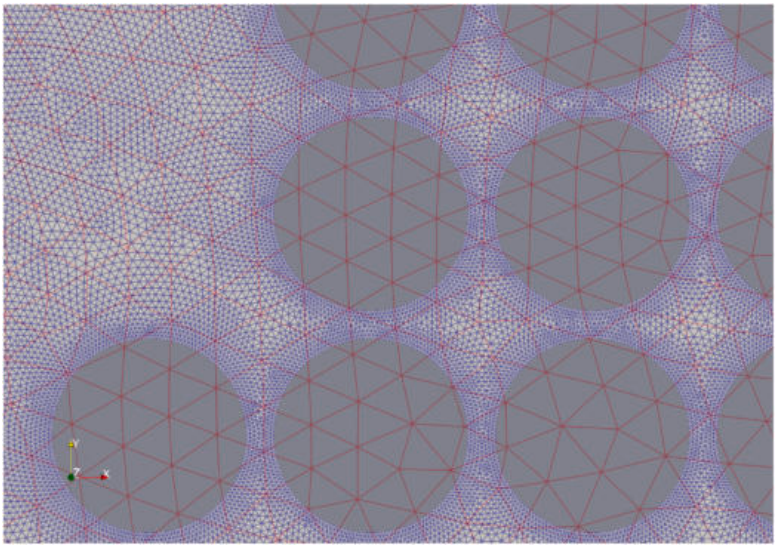

Fig. 3. The computational grid of the PSSs (blue) and the $\mathcal{G}_f$ grid for the filtering operations (red).

a truncated Gaussian filter, with the kernel clipped at a distance of $2l_\mathcal{V}$ from the center. Given the rapid decay of the Gaussian, the value at the cutoff is negligible ($< 1 \times 10^{-16}$), ensuring that the normalization condition is preserved and no significant numerical errors are introduced.

In general, for a robust filter of suitable size, the filtered (macroscopic) variables within the averaging volume should exhibit negligible fluctuations at scales smaller than the REV size. In the case of porosity, this implies that the computed filtered value should equal ϕ_0 in the core of the porous medium. In a preliminary test, we compared the bulk porosity computed using the aforementioned filters. The Gaussian filter proved more robust than the other three, producing negligible oscillations of ϕ_0 within the REV for $l_\mathcal{V} \geq 2ul$, whereas non-negligible fluctuations were observed with the cellular, quartic, and top-hat filters, even at larger $l_\mathcal{V}$ values. These observations partially agree with the results reported in [25].

Based on these preliminary analyses, we adopted the Gaussian filter for the subsequent filtering operations, whose 1D form is (see [25] and Fig. 1):

$$G(y, l_\mathcal{V}) = \frac{\sqrt{2.9548}}{l_\mathcal{V}/2} \exp\left(\frac{-2.9548\, y^2}{(l_\mathcal{V}/2)^2}\right).$$

The filter size $l_\mathcal{V}$ was varied such that $2ul \leq l_\mathcal{V} \leq 5ul$.

We averaged (filtered) the PSS results in the rectangular cyan area in Fig. 2 (top row), of size $100ul \times 50ul$, discretized using an unstructured grid denoted as $\mathcal{G}_f$ with mean element size $h = 0.228ul$ (see Fig. 3). The centroids of the averaging (filtering) volumes correspond to the centroids of the triangles of $\mathcal{G}_f$. The rationale behind the choice of $\mathcal{G}_f$ grid size is discussed in Section 4.1.

Using the same h range, for several values of $Re \in [10, 40]$, we performed PSSs over a larger computational domain ($L_1 = 40D$, $L_2 = 15D$, $L_3 = 20D$). The (dimensionless) integrals of the force $\mathbf{F}_d$ acting on the porous cylinder, as defined in Eq. (5), are reported in Table 2. Since the maximum difference was approximately 2.07%, we concluded that the original computational domain extent was adequate.

Let $\mathcal{I}$ denote the "ideal" interface with no thickness between the fluid region and the porous cylinder, located at a distance $D/2$ from the cylinder center (see Fig. 2, bottom row, right). The unit vectors $\mathbf{n}$ and $\boldsymbol{\tau}$ define the directions orthogonal and tangential to $\mathcal{I}$, respectively.

Table 2
Values of the integral over the porous cylinder of the force $\mathbf{F}_d$ in Eq. (5) computed in the original and larger domains. Values made dimensionless dividing by $D/U_{x,0}^2$.

	Original Domain			Larger Domain		
Re	M1	M2	M3	M1	M2	M3
10	0.7532	0.9257	1.04258	0.7547	0.9278	1.0439
25	0.4812	0.5905	0.68100	0.4822	0.5895	0.68175
40	0.4013	0.4876	0.56820	0.4020	0.4868	0.56750

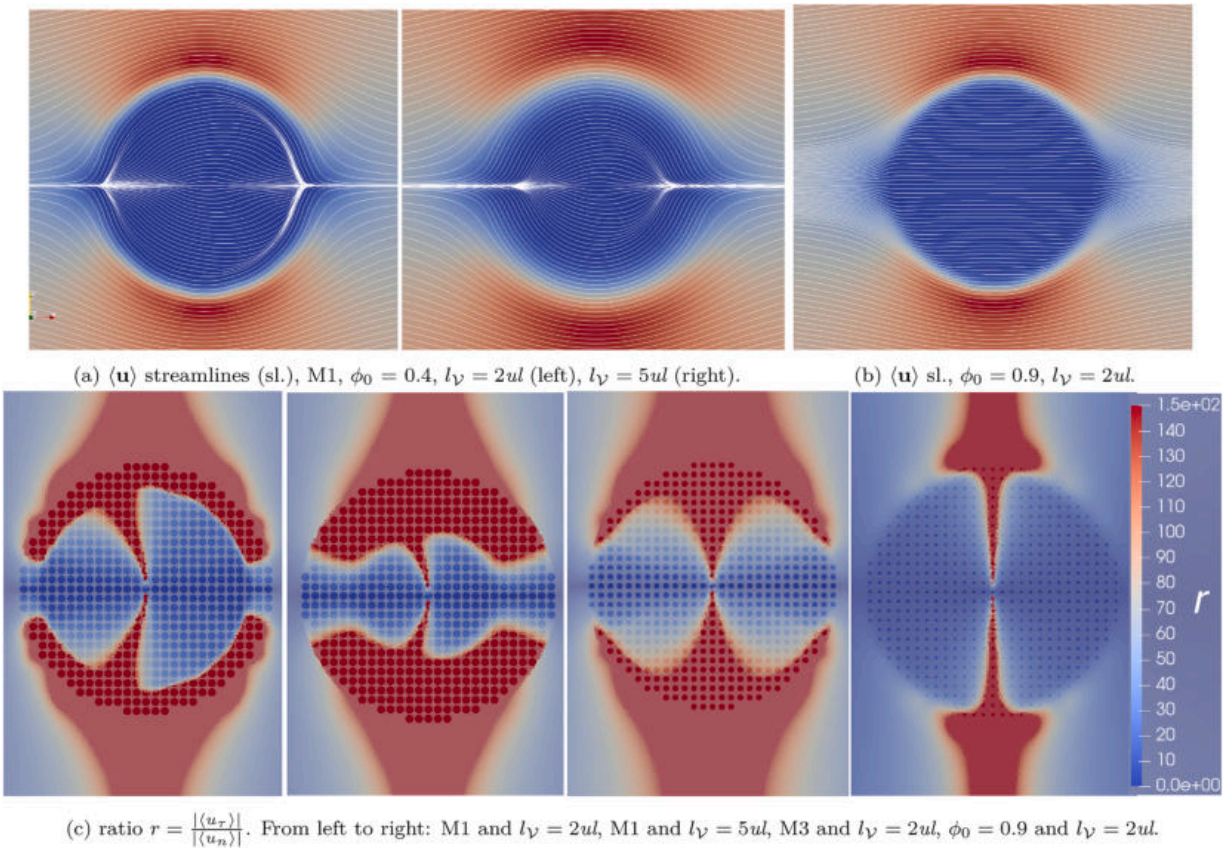

(a) $\langle \mathbf{u} \rangle$ streamlines (sl.), M1, $\phi_0 = 0.4$, $l_{\mathcal{V}} = 2ul$ (left), $l_{\mathcal{V}} = 5ul$ (right). (b) $\langle \mathbf{u} \rangle$ sl., $\phi_0 = 0.9$, $l_{\mathcal{V}} = 2ul$.

(c) ratio $r = \frac{|\langle u_\tau \rangle|}{|\langle u_n \rangle|}$. From left to right: M1 and $l_{\mathcal{V}} = 2ul$, M1 and $l_{\mathcal{V}} = 5ul$, M3 and $l_{\mathcal{V}} = 2ul$, $\phi_0 = 0.9$ and $l_{\mathcal{V}} = 2ul$.

Fig. 4. $\langle \mathbf{u} \rangle$ streamlines and ratio $r = \frac{|\langle u_\tau \rangle|}{|\langle u_n \rangle|}$ for different porous materials and REV sizes.

We assumed that the principal anisotropy directions of permeability are aligned with $\mathbf{n}$ and $\boldsymbol{\tau}$, rotated anticlockwise by an angle θ relative to the x-axis (see Fig. 2, bottom right). Physically, by adopting a curvilinear anisotropic framework, the model captures both viscous shear along the tangential direction of the cylinder and pressure-driven filtration in the normal direction.

Accordingly, we rewrite Eq. (6) as (e.g., [43]):

$$\mathbf{R}\,\tilde{\mathbf{K}}(\mathbf{x})^{-1}\,\mathbf{R}^{-1}\,\nu\,\phi(\mathbf{x})\,\langle \mathbf{u} \rangle = \mathbf{F}_d, \tag{7}$$

where $\mathbf{R}$ is the rotation matrix and $\tilde{\mathbf{K}}(\mathbf{x})^{-1}$ is diagonal:

$$\mathbf{R} = \begin{pmatrix} \cos\theta & \sin\theta \\ -\sin\theta & \cos\theta \end{pmatrix}, \quad \tilde{\mathbf{K}}(\mathbf{x})^{-1} = \begin{pmatrix} \tilde{k}_n(\mathbf{x})^{-1} & 0 \\ 0 & \tilde{k}_\tau(\mathbf{x})^{-1} \end{pmatrix}.$$

Here, $\tilde{k}_n(\mathbf{x})^{-1}$ and $\tilde{k}_\tau(\mathbf{x})^{-1}$ are the inverses of the permeability coefficients along the principal anisotropy directions. Left-multiplying both sides by $\mathbf{R}^{-1}$ yields:

$$\tilde{\mathbf{K}}(\mathbf{x})^{-1}\,\mathbf{R}^{-1}\,\nu\,\phi(\mathbf{x})\,\langle \mathbf{u} \rangle = \mathbf{R}^{-1}\mathbf{F}_d, \tag{8}$$

where $\mathbf{R}^{-1}\,\nu\,\phi(\mathbf{x})\,\langle \mathbf{u} \rangle$ and $\mathbf{R}^{-1}\mathbf{F}_d$ are vectors expressed in the tangential-normal $(\mathbf{n}, \boldsymbol{\tau})$ system.

As shown in Fig. 4(a) and Fig. 4(b), the velocity streamlines crossing the porous cylinder for materials M1, M2, and M3 are nearly tangential to $\mathcal{I}$, except in small regions near the front and back faces of the cylinder ($\theta \simeq 0$ and $\theta \simeq \pi$; see Fig. 2, bottom right). In Fig. 4(a), the streamlines for M1 with $l_{\mathcal{V}} = 2ul$ (left) and $l_{\mathcal{V}} = 5ul$ (right) are shown. Increasing $l_{\mathcal{V}}$ generally produces a smoothing effect near $\mathcal{I}$ because velocity and pressure values in the porous medium are filtered with a larger set of values from the fluid region, and vice versa.

Horizontal flow lines are typically associated with higher material porosity/permeability. For example, in Fig. 4(b), streamlines obtained from PSSs with the same numerical settings and $\phi_0 = 0.9$ are shown. In Fig. 4(c), we plot the ratio

$$r = \frac{|\langle u_\tau \rangle|}{|\langle u_n \rangle|}$$

between the tangential and normal components of the surface-averaged velocity. For M1 with $l_{\mathcal{V}} = 2ul$, $r \gg 1$ near $\mathcal{I}$. Increasing $l_{\mathcal{V}}$ from $2ul$ to $5ul$ decreases r in the fluid region while increasing it within the porous matrix. This reflects the smoothing effect of larger

Table 3
Computed values of K_0 and Darcy number for materials 1–3 and the material with $\phi_0 = 0.9$.

Material	ϕ_0	K_0 [m^2]	Da_0 [—]
1	0.40	2.50×10^{-10}	1.35×10^{-06}
2	0.50	9.01×10^{-10}	4.95×10^{-06}
3	0.65	3.15×10^{-09}	1.73×10^{-05}
extra	0.90	$\simeq 1.7 \times 10^{-08}$	$\simeq 1.00 \times 10^{-04}$

Table 4
Computed values of K_0 for materials 1–3 over the computational grids in Section 3.1 and the associated relative errors.

	M1		M2		M3	
Grid	K_0 [m^2]	err_{K_0} [%]	K_0 [m^2]	err_{K_0} [%]	K_0 [m^2]	err_{K_0} [%]
Coarse	2.550×10^{-10}	–	9.019×10^{-10}	–	3.212×10^{-09}	–
Medium	2.500×10^{-10}	1.961	9.010×10^{-10}	1.932	3.150×10^{-09}	1.921
Fine	2.468×10^{-10}	1.280	8.894×10^{-10}	1.292	3.110×10^{-09}	1.283

filter sizes. Increasing the bulk porosity ϕ_0 (from M1 to M3) reduces the region near $\mathcal{I}$ where $r \gg 1$. For $\phi_0 = 0.9$, $r \gg 1$ only in small regions near $\theta \simeq \pi/2$ and $\theta \simeq 3\pi/2$ (last panel in Fig. 4(c)).

The previous discussion on the ratio of the velocity components near the interface $\mathcal{I}$ motivates our choice in computing the permeability tensor coefficients. In this work, we focus on cases where the condition $|\langle u_n \rangle| \ll |\langle u_\tau \rangle|$ holds close to the interface. Under this hypothesis, we consider only the component of Eq. (8) along the $\boldsymbol{\tau}$ direction, i.e.,

$$\left(\tilde{k}_\tau(\mathbf{x})\right)^{-1} \nu\, \phi(\mathbf{x}) \left(\cos\theta\, \langle u_x \rangle + \sin\theta\, \langle u_y \rangle\right) = \cos\theta\, F_{d,x} + \sin\theta\, F_{d,y}, \tag{9}$$

and we define $\left(\tilde{k}_\tau(\mathbf{x})\right)^{-1} = \mathfrak{K}(\mathbf{x})$, the inverse of the tangential permeability coefficient:

$$\mathfrak{K}(\mathbf{x}) = \frac{\cos\theta\, F_{d,x} + \sin\theta\, F_{d,y}}{\nu\, \phi(\mathbf{x}) \left(\cos\theta\, \langle u_x \rangle + \sin\theta\, \langle u_y \rangle\right)}. \tag{10}$$

Physically, this implies that momentum dissipation at the fluid-porous interface is dominated by tangential shear stress rather than the impact of the normal flow on the cylinder surfaces.

Our assumptions depart from the conventional practice of aligning the principal anisotropy directions along the x and y axes. Using a Cartesian alignment would introduce an artificial resistance because the model would assume that the fluid impacts the solid inclusions along an unphysical direction. In contrast, our choice of aligning the principal anisotropy directions with the local tangential and normal directions yields a more physically consistent description. Numerical results at the mesoscopic averaged scale, obtained using the procedure described below, are reported in Appendix C.

The bulk permeability values $K_0 = \mathfrak{K}_0^{-1}$ computed for materials M1, M2, M3, and the material with $\phi_0 = 0.9$, along with the associated Darcy numbers $Da_0 = K_0/D^2$, are listed in Table 3. In Table 4, we compare the bulk permeability obtained on coarse, medium, and fine grids (see Section 3.1) and report the relative errors. As mentioned in Section 3.1, the relative error between the fine and medium grids is below 1.3%, indicating that the medium grid is sufficient for the PSSs and filtering operations, and finer grids do not significantly change the computed permeability values.

The bulk permeability values K_0 in Table 3 are generally consistent with literature data [44,45] for infinite arrays of cylinders (flow perpendicular to the cylinder axis). Relative differences with [45] range from 3% to 24% as the porosity increases from 0.4 to 0.9, while the opposite trend is observed with [44]. These discrepancies likely arise from the simplified analytical approaches in the literature papers. The solution in [44] uses series expansions for infinite periodic arrays, accurate for moderate solid fractions but potentially divergent for closely packed cylinders due to strong interactions. Wang [45] employs coupling methods or series expansions that may be affected by truncation errors or different boundary condition assumptions.

In Fig. 5, we show the dimensionless profiles of ϕ and $\mathfrak{K}$ across $\mathcal{I}$ for materials M1, M2, and M3, using different REV sizes. The distance d from $\mathcal{I}$ and $\mathfrak{K}$ are made dimensionless by $l_\mathcal{V}$ and the bulk value $\mathfrak{K}_0$, respectively. The profiles cluster closely; for clarity, we show only $l_\mathcal{V} = 2ul$ and $l_\mathcal{V} = 5ul$, with intermediate REV sizes falling in between. A key physical feature emerging from the filtering of PSSs is that the porosity $\phi(d)$ and $\mathfrak{K}(d)$ distributions exhibit shifted profiles relative to each other. While the porosity transition is governed by the geometric arrangement of the solid phase, the $\mathfrak{K}$ profile is shifted toward the inner porous domain. This indicates that the maximum hydrodynamic resistance (bulk value) is not attained abruptly at the geometric interface, but develops over a finite depth within the matrix. Physically, this occurs because the flow in the peripheral layers of the porous cylinder experiences a “lateral relief” due to the proximity of the free-fluid region, which locally reduces momentum exchange constraints and viscous dissipation. Consequently, the effective drag starts to decrease while still within the solid boundaries, a phenomenon that must be explicitly captured to avoid the unphysical drag overestimation typical of penalized models. Similar trends are reported in [23–25]. Non-monotonic profiles in some of these literature studies likely reflect the use of different filters, such as cellular or top-hat filters.

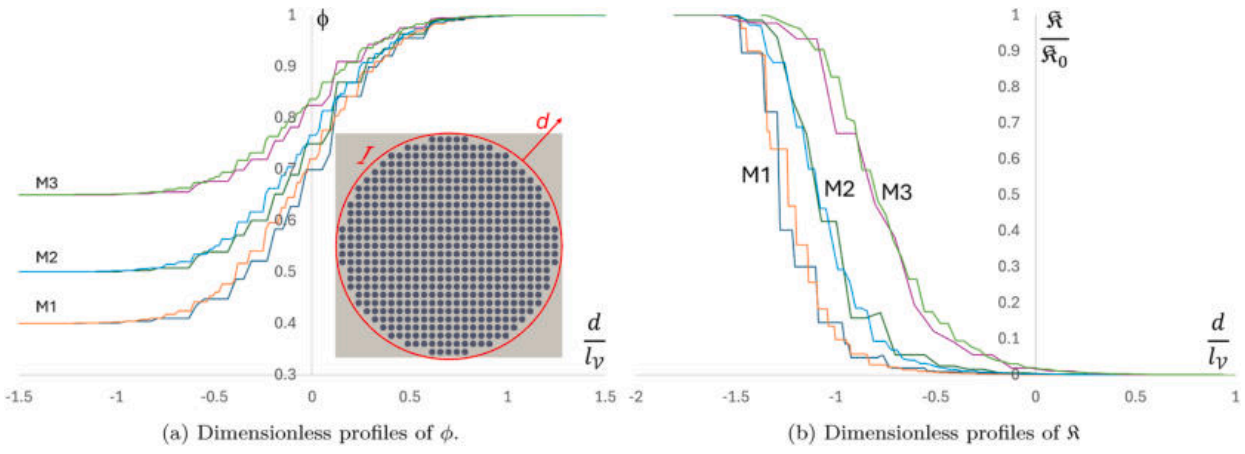

(a) Dimensionless profiles of ϕ. (b) Dimensionless profiles of $\mathfrak{K}$

Fig. 5. Dimensionless profiles of ϕ and $\mathfrak{K}$ across the interface $\mathcal{I}$.

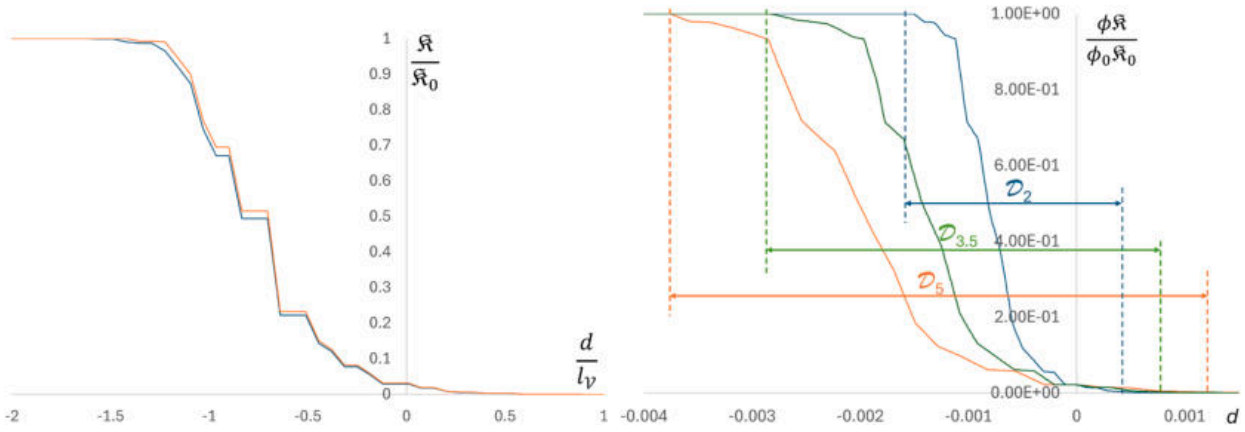

Fig. 6. Material M3, left) dimensionless profiles of $\frac{\mathfrak{K}}{\mathfrak{K}_0}$ for $Re \simeq 13$ and $Re \simeq 130$; right) profiles of $\frac{\phi\mathfrak{K}}{\phi_0\mathfrak{K}_0}$ and the associated extents $\mathcal{D}_n$ given by Eq. (11).

Although the preliminary PSSs are computationally expensive, they constitute a "one-time investment" over a representative domain. Modern high-performance computing resources make these calculations feasible. As shown in Figs. 5 and 6 (left), ϕ and $\mathfrak{K}$ exhibit good scalability. Once characterized, these profiles can be applied in large-scale simulations where full pore-scale resolution is computationally prohibitive. In contrast, approaches based on Ergun-type equations [37] impose permeability and porosity variations over the same interval, which does not capture the observed shift between ϕ and $\mathfrak{K}$ near the interface.

Qualitatively, the trend of our permeability profiles (Fig. 5(b)) resembles those in [27], where resistance decreases with increasing porosity. The permeability there was obtained from a Local Closure Problem of a Generalized Transport Equation under the length scale constraints in Section 2. In contrast, Hernandez-Rodriguez et al. [28] observed strong REV-size dependence and discontinuities when filtering PSS results.

Generally, $\phi \to 1$ for $d/l_{\mathcal{V}} \geq 1$ and $\phi \to \phi_0$ for $d/l_{\mathcal{V}} \leq -1$, while $\mathfrak{K} \to 0$ for $d/l_{\mathcal{V}} \geq 0.5$ and $\mathfrak{K} \to \mathfrak{K}_0$ for $d/l_{\mathcal{V}} \leq -1.5$. The transition zone for ϕ and $\mathfrak{K}$ thus spans approximately $2\ d/l_{\mathcal{V}}$, depending on the REV size. Consequently, $\phi\,\mathfrak{K}$ in Eq. (6) varies between 0 and $\phi_0\mathfrak{K}_0$. With the chosen $\mathcal{G}_f$ grid, the transition zone is covered by approximately 17–44 averaging volumes for $l_{\mathcal{V}} \in [2ul, 5ul]$, ensuring good spatial resolution.

The permeability profiles are insensitive to the macroscopic Reynolds number (Section 3.1). For example, in Fig. 6 (left), $\mathfrak{K}/\mathfrak{K}_0$ profiles for M3 at $Re \simeq 13$ and $Re \simeq 130$ nearly coincide, confirming that inertial effects are negligible within the porous obstacle.

Let D_n denote the extent of the transition zone where $\phi\,\mathfrak{K}$ varies continuously across the interface for REV size $l_{\mathcal{V}} = nul$. We define $\tilde{D} = D_2$ and $\tilde{n} = 2$. Then, in general,

$$D_n = \tilde{D}\,\frac{2nul}{2\tilde{n}ul}. \tag{11}$$

In Fig. 6 (right), we plot dimensionless profiles of $\phi\,\mathfrak{K}$ and the associated extents $\mathcal{D}_n$ for $n = 2, 3.5, 5$ for material M3 across $\mathcal{I}$.

4. Steady flow around and within a circular porous cylinder

In this section, the interaction between an unconfined flow and a circular porous cylinder is analyzed at the mesoscopic averaged scale. The study focuses on the structure of the recirculating wake behind the porous body and the forces acting on it. To obtain a reference solution, the same configuration was simulated at the pore scale, with results averaged (filtered) according to the procedure described in Section 3.2. To limit the computational cost of the PSSs, the cylinder diameter was set to $D = 19ul$, maintaining $ul = 0.0005$ m, and the same materials M1, M2, and M3. The problem setup is identical to that in Fig. 2.

The problem is made dimensionless by choosing characteristic scales for length, D, velocity, $U_{x,0}$, time, $D/U_{x,0}$, and kinematic pressure, $U_{x,0}^2$. The dimensionless form of the pore-scale governing equations Eq. (1) is

$$\nabla^* \cdot \mathbf{u}^* = 0, \tag{12a}$$

$$\frac{\partial \mathbf{u}^*}{\partial t^*} + \mathbf{u}^* \cdot \nabla^* \mathbf{u}^* = -\nabla^* \Psi^* + \frac{1}{Re} \nabla^{*2} \mathbf{u}^*, \tag{12b}$$

while the dimensionless form of the averaged governing equations Eq. (4) with the closure in Eq. (6) reads:

$$\nabla^* \cdot \langle \mathbf{u} \rangle^* = 0, \tag{13a}$$

$$\frac{\partial \langle \mathbf{u} \rangle^*}{\partial t^*} + \langle \mathbf{u} \rangle^* \cdot \nabla^* \left(\frac{\langle \mathbf{u} \rangle^*}{\phi} \right) = -\phi \nabla^* \langle \Psi \rangle^{i*} + \frac{1}{Re} \nabla^{*2} \langle \mathbf{u}^* \rangle + \frac{\phi \langle \mathbf{u} \rangle^*}{Re\, Da}, \tag{13b}$$

where the symbol $*$ denotes dimensionless variables. The term $Da = \mathfrak{K}^{-1}/D^2$ in Eq. (13b) can be regarded as a "position-dependent" Darcy number, since it varies across the interface $\mathcal{I}$ according to the local variation of $\mathfrak{K}$.

To ensure steady-state conditions, the Reynolds number, computed as in Section 3.1, was limited to $Re \leq 40$. For $Re > Re_0$, a steady, symmetric recirculating wake forms downstream of the cylinder. The critical Reynolds number Re_0 was approximately in the ranges $5.8 \leq Re_0 \leq 6.25$ for M1, $7 \leq Re_0 \leq 7.5$ for M2, and $8.2 \leq Re_0 \leq 8.8$ for M3. The wake size increases with Re.

Eqs. (12) and (13) were solved using the in-house numerical scheme recently proposed and validated in [42]. For the mesoscopic averaged-scale simulations, we used the same bulk values ϕ_0 and $\mathfrak{K}_0$, and implemented the transition-zone profiles $\phi(d)$ and $\mathfrak{K}(d)$ directly in the numerical solver (see Fig. 5).

The variation of the transition zone extent D_n and the profiles $\phi(d)$ and $\mathfrak{K}(d)$ obtained with different REV sizes $l_\mathcal{V}$ (see Section 3.2) effectively "mimics" the change of porous medium properties near the interface. From now on, $\mathcal{P}_n^*$ denotes the profile of $\phi(d^*)/Re\, Da(d^*)$ associated with REV size $l_\mathcal{V} = nul$ (d^* is the dimensionless distance from the idealized interface $\mathcal{I}$), and D_n^* is the dimensionless extent of the transition zone. We define $\tilde{D}^* = D_2^*$ corresponding to the minimum REV size. For example, in Fig. 7 the profiles $\mathcal{P}_n^*$ for material M1 at $Re = 15$ are shown for $l_\mathcal{V} = 2ul$ and $3.5ul$. The dark gray line represents a penalized approach with a sharp discontinuity at the interface, in which ϕ and Da take their bulk values in either the porous or fluid region. Moving toward the cylinder core, $\mathcal{P}_{3.5}^*$ emulates a medium with lower resistance than $\mathcal{P}_2^*$, while the penalized framework represents maximum resistance.

From these considerations, the wake behind the cylinder, and more generally the flow field computed by the mesoscopic averaged-scale model, depends not only on the computational grid size but also on the REV size used to filter the PSS output, which determines the profiles $\mathcal{P}_n^*$ and thus mimics different effective porous properties.

To study these effects separately, we proceed as follows:

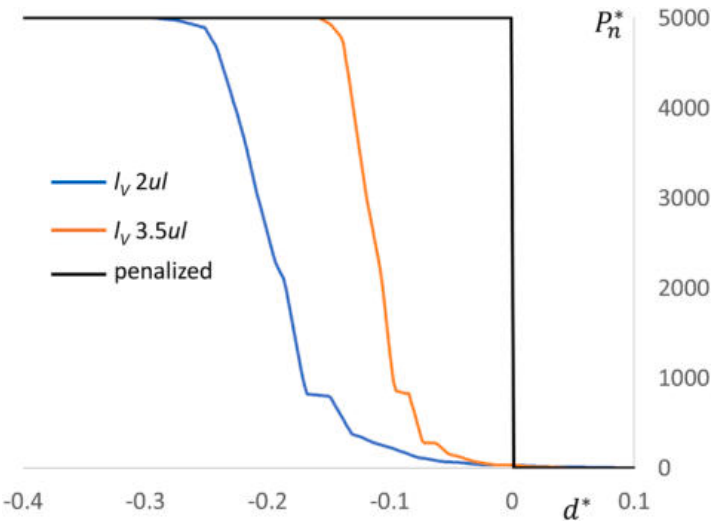

Fig. 7. P_n^* associated with $l_\mathcal{V} = 2ul$, $l_\mathcal{V} = 3.5ul$ and in the case of the penalized approach.

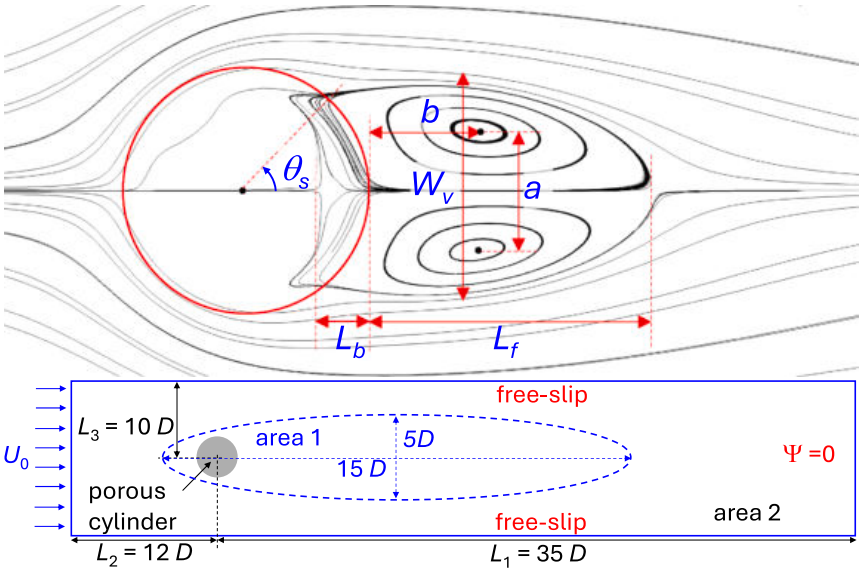

(a) Investigated wake geometrical parameters (top row); settings of the numerical experiments for the solid and porous cylinder simulations (bottom row).

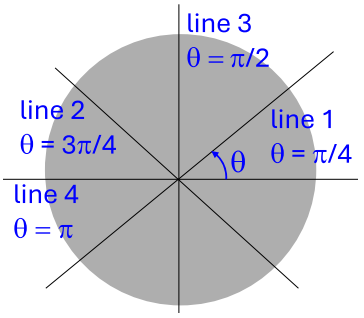

(b) Lines along which we compute the profiles of $\langle u_x \rangle^*, \langle u_y \rangle^*$ and $\langle \Psi \rangle^{i,*}$ in Section 4.2.2.

Fig. 8. Parameters of the wake and setup of the numerical experiments.

- In Section 4.1, we perform a sensitivity analysis of the recirculating wake structure to the grid size for a solid cylinder, using the same setup as in Fig. 2. Literature data are available for validation. This analysis identifies the optimal grid size for subsequent mesoscopic simulations of a porous cylinder.
- In Section 4.2, we investigate the combined effects of grid resolution and the profiles of porosity and permeability across the interface, associated with different REV sizes, on the wake structure and overall flow field.

The geometrical parameters describing the recirculating wake are shown in Fig. 8(a) (top row): the downstream vortex length L_f, the penetration length L_b inside the cylinder, the maximum vertical wake extent W_v, the x-coordinates of the vortex centers b and their vertical separation a. The separation angle θ_s is only considered for a solid cylinder, since no wake originates directly from the surface of a porous cylinder.

The boundary conditions for the averaged-scale simulations are similar to those in the PSSs (see Fig. 8(a), bottom row): imposed undisturbed velocity at the upstream boundary, zero kinematic pressure at the downstream boundary, and free-slip conditions at the top and bottom domain boundaries.

4.1. *Sensitivity analysis of the recirculating wake to the grid size. The case of the solid cylinder and validation with literature data*

The computational domain was discretized using different grid resolutions in "area 1" and "area 2", as shown in Fig. 8(a) (bottom row). The sensitivity analysis indicated that using a coarse grid ($h^* = 0.65$) in area 2 did not significantly affect the wake structure or its size. To ensure accuracy in the near-field, a refinement study was conducted in area 1. Table 5 compares the computed drag coefficient C_D, separation angle θ_s, and vortex wake length L_f (see Fig. 8(a), top row) with existing experimental and numerical results from the literature [8,46–49].

Our solver achieved good agreement with these benchmarks using a dimensionless grid size of $h^* = 0.012$ in area 1. Further refinement ($h^* < 0.012$) did not produce significant changes in the results. The influence of grid resolution increases with Re, which can be explained by the fact that at higher Re, the recirculating wake expands downstream, producing larger gradients in both pressure and velocity components, thus requiring finer resolution to accurately capture these variations.

4.2. *Analysis of the recirculating wake structure and of the flow field around and crossing the porous cylinder*

This section investigates, at the mesoscopic averaged scale, how the computational grid size and the extent of the transition zone $\mathcal{D}_n^*$ across the interface $\mathcal{I}$, along with its associated profile $\mathcal{P}_n^*$, affect the structure of the recirculating wake and the overall flow field around the porous cylinder. The analysis is structured as follows:

- In Section 4.2.1, using a fixed computational grid size, we investigate the effects of varying the transition zone extent $\mathcal{D}_n^*$ and the corresponding profiles $\mathcal{P}_n^*$, associated with different REV sizes. These variations emulate changes in the porous medium properties near the interface $\mathcal{I}$.

Table 5
Computed values of C_D, θ_s and (dimensionless) L_f. Case of a solid cylinder.

Re	Model/Reference	C_D	θ_s [°]	L_f
10	**Present model**	–	27.95	0.245
	Sen et al. [49]	–	27.95	0.244
20	**Present model**	2.038	43.11	0.918
	Sen et al. [49]	–	42.51	0.912
	Yu et al. [8]	2.040	43.31	0.916
	Coutanceau [46]	–	44.80	0.930
	Fornberg [47]	2.000	–	0.910
	Dennis [48]	2.045	43.70	0.940
30	**Present model**	–	49.12	1.496
	Sen et al. [49]	–	48.95	1.580
40	**Present model**	1.518	53.10	2.246
	Sen et al. [49]	–	52.80	2.248
	Yu et al. [8]	1.523	53.71	2.236
	Coutanceau [46]	–	53.50	2.130
	Fornberg [47]	1.498	–	2.240
	Dennis [48]	1.522	53.80	2.345

- In Section 4.2.2, we study the combined effects of changes in the grid size and the transition zone extent $\mathcal{D}_n^*$ with its associated profiles $\mathcal{P}_n^*$.

The averaged (filtered) PSSs, which serve as reference solutions, were obtained using the smallest considered REV size, $l_\mathcal{V} = 2ul$, in order to prevent over-smoothing of the velocity and pressure fields near the interface, as discussed in Section 3.2. Filtering the PSS results using larger REV sizes can significantly affect the structure and size of the filtered wake, particularly for $Re \leq 10$. Due to these over-smoothing effects, the vortical structures vanish when the REV size increases from $l_\mathcal{V} = 2ul$ to $l_\mathcal{V} = 5ul$, as illustrated in Fig. 9.

Numerical simulations were also performed using the penalized approach (see Section 1). These solutions were computed using the same numerical solver [42], imposing a sharp jump in ϕ and $\mathfrak{K}$ at the interface $\mathcal{I}$. Hereafter, the mesoscopic averaged-scale ODA solver and the penalized approach are referred to as "MSODA" and "PODA", respectively.

For the present application, some benchmark data are available in the literature within the penalized framework, as specified in Section 1. In Appendix D, we compare the results obtained using the solver [42] in the PODA framework with corresponding literature data.

4.2.1. The effects of the variation of the transition zone extent $\mathcal{D}_n^*$ and the associated profile $\mathcal{P}_n^*$, depending on different REV sizes $l_\mathcal{V}$

Assuming a dimensionless grid size of $h^* = 0.012$ in area 1 of the computational domain (as established in Section 4.1), Figs. 10 to 14 (left) shows, for material M1, the Re-dependent trends of L_f, a, b, W_V, L_b as predicted by the PODA and MSODA solvers, compared with the reference filtered solution. The MSODA results were obtained using the transition zone extents $\mathcal{D}_n^*$ and associated profiles $\mathcal{P}_n^*$ with $2 \leq n \leq 5$. Similar trends were observed for materials M2 and M3 (omitted for brevity). The following observations are derived from the analysis:

- For a fixed Re, the recirculating wake generally expands with increasing $l_\mathcal{V}$. Specifically, the wake front L_f extends further downstream, the vertical vortex width W_V increases, the vortex center moves outward, and the penetration length L_b within the cylinder increases. The values of W_V computed for $Re = 10$ (Fig. 13) are approximate, as the vortex is very close to the cylinder surface, making it difficult to estimate from the velocity field. Based on Fig. 7, larger $l_\mathcal{V}$ corresponds to a smaller "mimicked" resistance of the porous medium. Physically, a smoother transition zone allows higher momentum transfer between the free fluid and the porous region, resulting in more extended wakes and larger vortices. Consequently, the averaged velocity components and kinetic energy within the porous region near $\mathcal{I}$ increase with $l_\mathcal{V}$. For example, Fig. 15 shows the profiles of $\langle u_x \rangle^*$ for M1 at $Re = 20$, along a $\theta = 3\pi/4$ oriented line, for $l_\mathcal{V} = 2ul$ and $l_\mathcal{V} = 5ul$ ($r^* = d^* + R^*$, with $R^* = D^*/2 = 0.5$, the dimensionless cylinder radius). Larger $l_\mathcal{V}$ also reduces velocity gradients, decreasing viscous shear forces and energy losses, allowing a larger downstream wake. Thus, the $\mathcal{P}_5^*$ velocity profile is smoother than $\mathcal{P}_2^*$, acting as a "hydrodynamic buffer" that preserves fluid kinetic energy. Conversely, the PODA solution underestimates the reference values of L_f, a, b, W_V, L_b, as the sharp interface restricts momentum transfer and produces higher viscous dissipation.
- The downstream penetration length, L_b, exhibits a non-monotonic trend with the Reynolds number (Re). Initially, L_b increases with Re as the recirculating wake strengthens, enhancing the suction effect at the rear stagnation point that draws fluid into the porous matrix from the downstream side. However, for $Re \gtrsim 25$–30, a slight reduction in L_b is observed. This behavior originates from the hydrodynamic competition between the upstream-directed recirculating flow and the high-momentum base flow entering from the front face. At lower Re, the wake-induced backflow expands significantly into the cylinder. Conversely, at higher Re, the increased momentum of the base flow penetrates deeper into the solid matrix, effectively acting as a hydraulic barrier that restricts the rear penetration zone and stabilizes the internal flow distribution. This trend agrees with [8], where a penalized approach was used with $Da_0 = 5 \times 10^{-6}$ and no significant differences were observed for $Da_0 \leq 1 \times 10^{-4}$. Their grid resolution was finer than in the present study (see Table 1 and Fig. 3 in [8]).

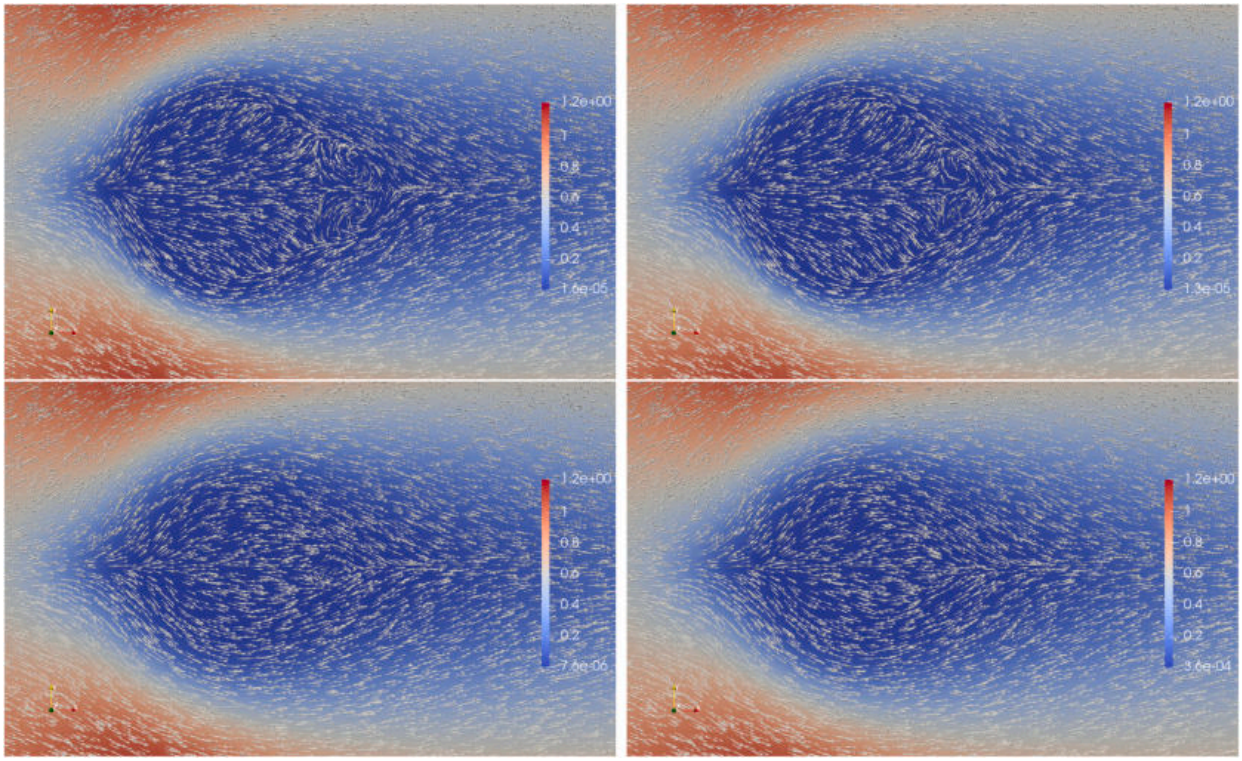

Fig. 9. Filtered velocity fields from PSSs, $Re = 10$. Materials M1 (left) and M3 (right). $l_{\mathcal{V}} = 2ul$ (top) and $l_{\mathcal{V}} = 5ul$ (bottom).

- The MSODA solution using the profiles $\mathcal{P}^*_{\tilde{n}}$ (smallest $l_{\mathcal{V}}$) closely matches the reference values for L_f, a, b, W_V, but slightly overestimates L_b. Using $\mathcal{P}^*_n$ with $n > 2$, the MSODA solution overestimates all variables relative to the reference.

The results suggest that the transition layer acts as a distributed momentum-exchange region. Increasing its thickness effectively reduces localized dissipation and enhances momentum penetration into the porous medium, leading to a larger wake extension.

Comparing the left and right panels of Figs. 10–14, the right panels show the same variables obtained by filtering PSS results with REV sizes $2ul \leq l_{\mathcal{V}} \leq 5ul$, using the same dimensionless grid size $h^* = 0.012$ as in area 1 for MSODA and PODA. The reference solution on the left corresponds to the filtered "$2ul$" solution on the right.

For $10 \leq Re \leq 40$, increasing $l_{\mathcal{V}}$ produces an opposite trend in the wake extent downstream of the cylinder compared to MSODA. Specifically, filtered PSS values of L_f, a, b, W_V decrease with $l_{\mathcal{V}}$, and for $Re = 10$ the vortical structures almost vanish when using $l_{\mathcal{V}} = 5ul$ (see Fig. 9). For this reason, $Re = 10$ results are omitted in the right panels. This could be related with the over-smoothing effects, mentioned before (see Section 3.2 and comments to Fig. 9). The sensitivity of the filtered geometrical variables to $l_{\mathcal{V}}$, particularly L_f and b, is smaller than in the MSODA solutions.

Remark 1. This analysis highlights a discrepancy between the volume-averaging framework and filtered PSS results. MSODA solutions using profiles $\mathcal{P}^*_n$ for increasing $l_{\mathcal{V}}$ show trends opposite to those observed in filtered PSS data obtained with the same REV and grid sizes.

This behavior contrasts with some previous studies on 1D flows (e.g., [28]), where MSODA velocity fields computed using porosity and permeability profiles from different REV sizes were consistent with filtered PSS results for the same REV.

In agreement with the MSODA results (Fig. 14, left), filtered PSS L_b values (Fig. 14, right) increase with $l_{\mathcal{V}}$. This may be attributed to the stronger effect of upstream-oriented velocity vectors in the fluid region ahead of the rear cylinder side, which have larger magnitudes than the velocities within the porous medium.

4.2.2. The combined effects of the variation of the grid size and the extent of the transition zone $\mathcal{D}^*_n$ with the associated profile $\mathcal{P}^*_n$, depending on different REV sizes $l_{\mathcal{V}}$

While grid coarsening reduces the wake size (Section 4.1), selecting a profile $\mathcal{P}^*_n$ associated with progressively larger REV sizes $l_{\mathcal{V}}$, which mimics a reduction in the resistance of the porous medium near the interface, produces the opposite effect (Section 4.2.1). In this section, we systematically investigate the combined influence of the computational grid size and the profile $\mathcal{P}^*_n$, aiming to minimize discrepancies between the MSODA predictions and the reference filtered PSSs, providing insight into the interplay between grid resolution and porous medium properties. At the end of the section, we also analyze the implications of these combined effects on the hydrodynamic forces acting on the cylinder.

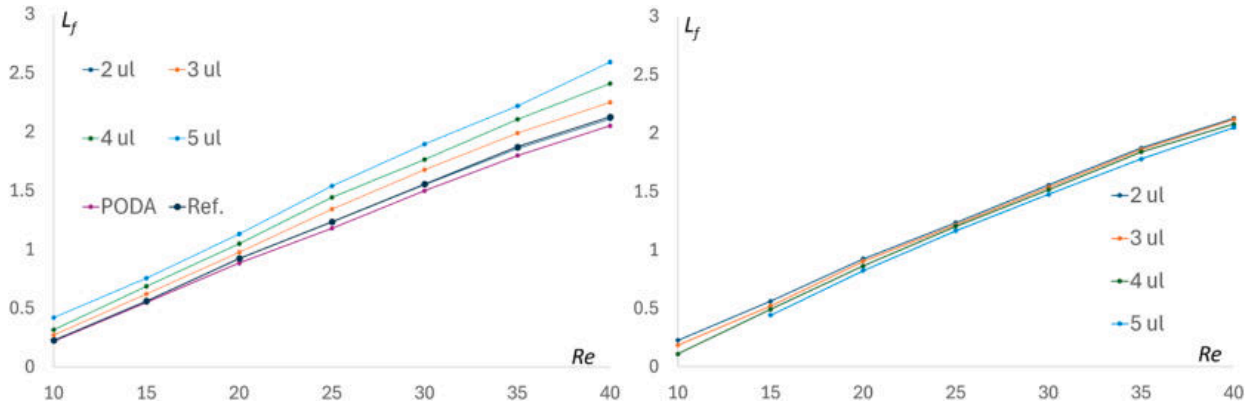

Fig. 10. (Dimensionless) wake parameter L_f. Results of the MSODA, PODA solvers and reference solution (left); averaged PSSs results (right), $10 \le Re \le 40$, (dimensionless) grid size $h^* = 0.012$, material M1 (the same applies in Figs. 11–14). Nomenclature (the same applies in Figs. 11–14): *nul*, with $2 \le n \le 5$, left) MSODA results with profiles $\mathcal{P}_n^*$, right) filtered PSSs results using REV sizes $2ul \le l_\mathcal{V} \le 5ul$.

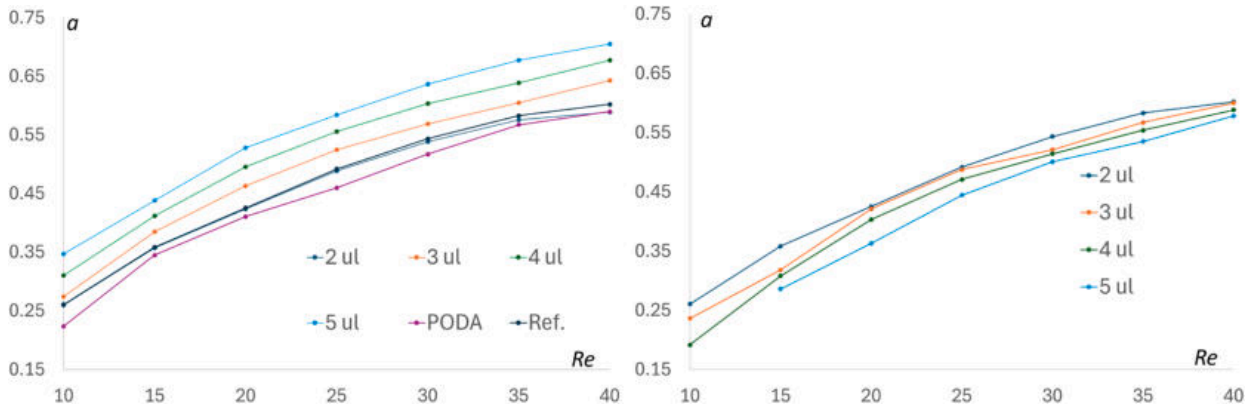

Fig. 11. (Dimensionless) wake parameter a.

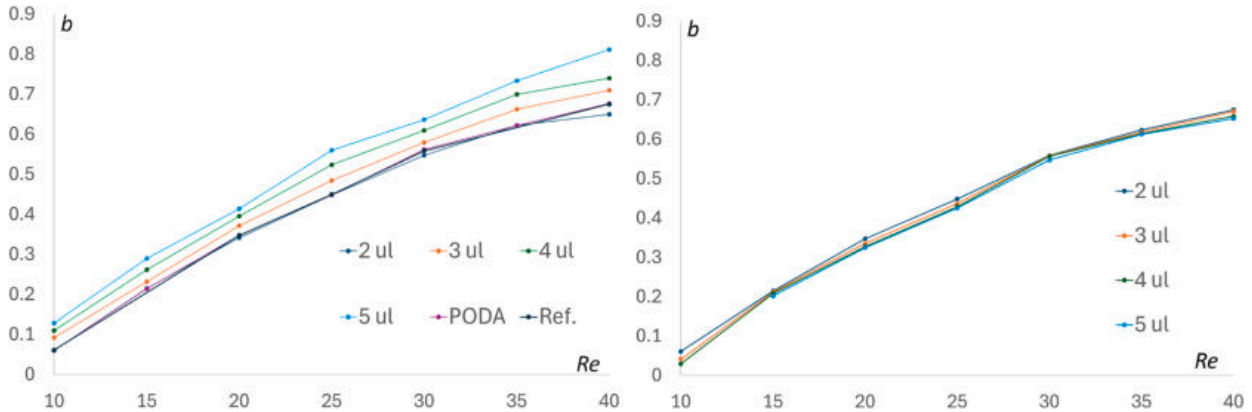

Fig. 12. (Dimensionless) wake parameter b.

For all simulations, the (dimensionless) grid size h^* is chosen so that the extent $\mathcal{D}_n^*$ of the transition zone across the interface $\mathcal{I}$, associated with a REV size $l_\mathcal{V} = nul$, is discretized with a constant number of grid elements. The specific h^* values for each $l_\mathcal{V}$ are reported in Table 6.

The profile $\mathcal{P}_n^*$ is modified by adjusting its transition zone extent according to

$$\mathcal{D}_n^* = \tilde{\mathcal{D}}^* \left(\frac{n}{\tilde{n}} \right)^\alpha, \qquad 0 \le \alpha \le 1, \tag{14}$$

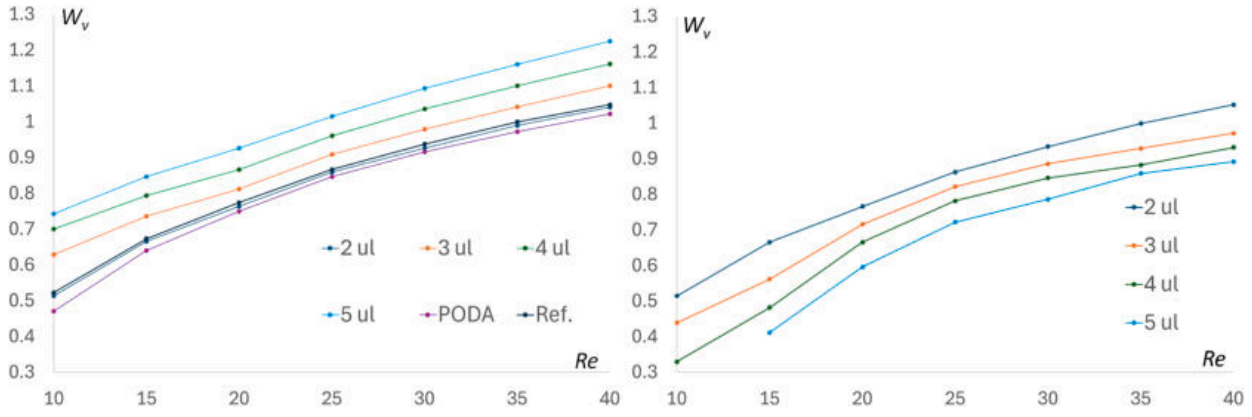

Fig. 13. (Dimensionless) wake parameter W_v.

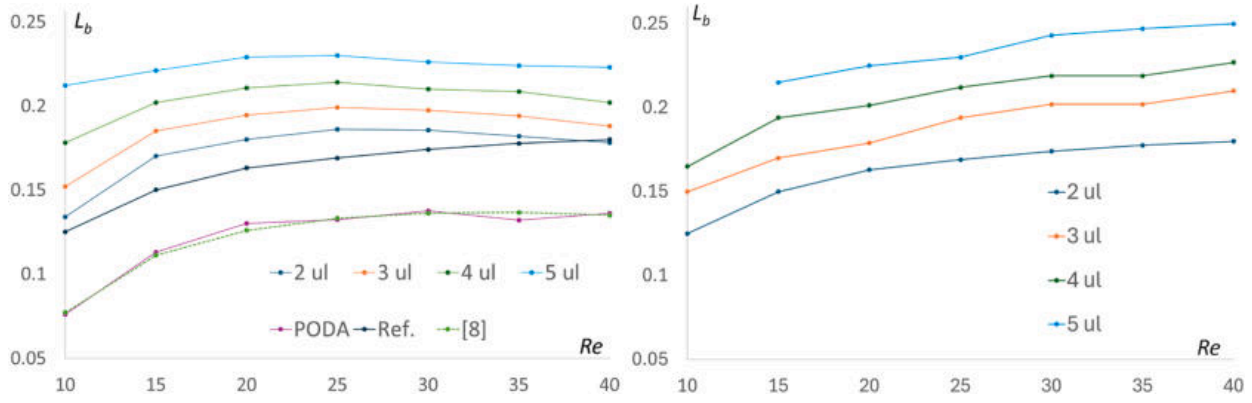

Fig. 14. (Dimensionless) wake parameter L_b. The results in [8], plotted in the left picture, pertain to a porous material with $Da_0 = 5 \cdot 10^{-06}$.

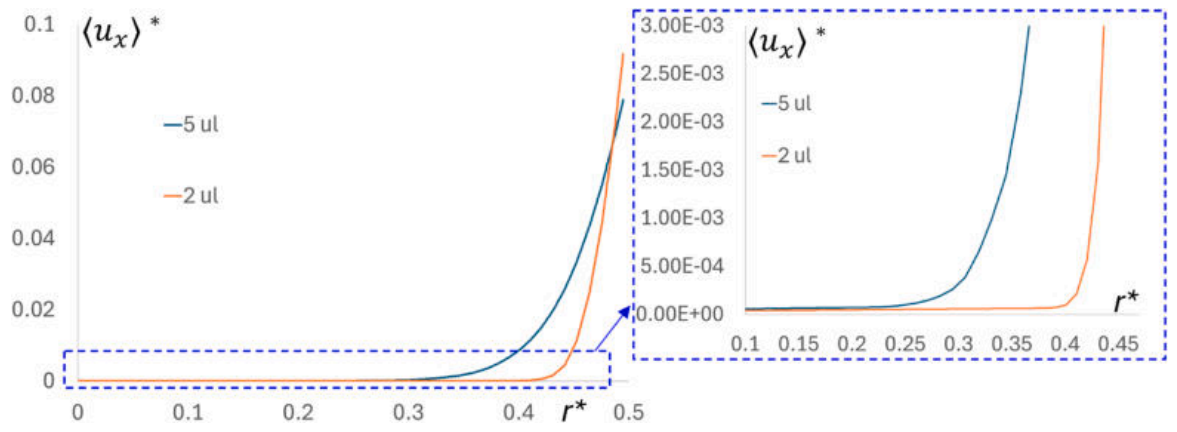

Fig. 15. Profiles of the computed $\langle u_x \rangle^*$ along a $\frac{3\pi}{4}$ degrees-oriented line, using $\mathcal{P}_5^*$ and $\mathcal{P}_2^*$, $Re = 20$, material M1. $r^* = d^* + R^*$.

where $\tilde{n} = 2$ denotes the minimum REV size. We denote by $\mathcal{P}_n^{\alpha,*}$ the corresponding profile of $\frac{\phi(d^*)}{Re\, Da(d^*)}$. The following points summarize the physical interpretation:

- For $n = \tilde{n}$, $\mathcal{P}_n^{\alpha,*} = \mathcal{P}_{\tilde{n}}^*$ for all $\alpha \in [0, 1]$.
- $\alpha = 1$ reproduces the filtered profile obtained via the standard procedure (Section 3.2) for different REV sizes ($2 \le n \le 5$), fully accounting for the change in porous material properties across the interface.
- $\alpha = 0$ enforces the same profile for all REV sizes, i.e., no variation of the porous medium properties is mimicked.

Table 6
REV size l_v and the associated dimensionless grid size h^*.

n	l_v	h^*
2	2.0ul	0.012
2.5	2.5ul	0.015
3	3.0ul	0.018
3.5	3.5ul	0.021
4	4.0ul	0.024
4.5	4.5ul	0.027
5	5.0ul	0.030

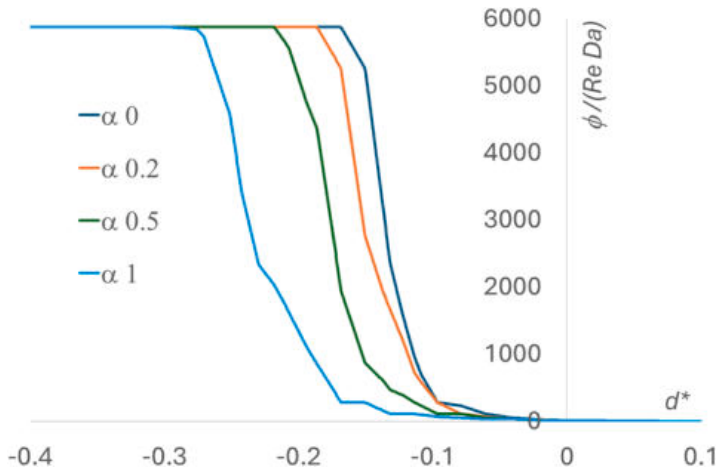

Fig. 16. Profiles $\mathcal{P}_{3.5}^{\alpha,*}$ for different values of power α in Eq. (14), $Re = 25$, material M1.

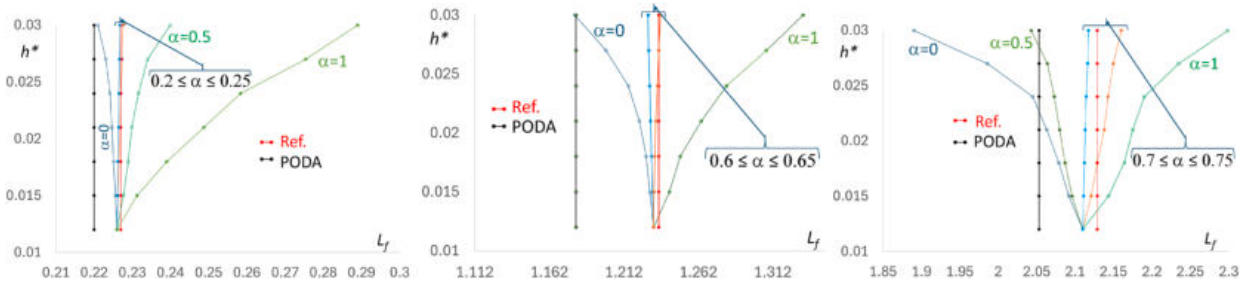

Fig. 17. Computed (dimensionless) L_f vs. h^*. From left to right, $Re = 10$, $Re = 25$, $Re = 40$, M1.

- For $n > 2$, decreasing α steepens $\mathcal{P}_n^{\alpha,*}$ (see Fig. 16), shifting the effective resistance closer to the interface. This emulates a progressively stronger opposition of the porous medium to the flow, with implications on momentum transfer and wake development.
- As n increases from 2 to 5 for any α, the number of grid points resolving the profile decreases, leading to a coarser discretization of the transition zone.

Multiple sets of MSODA simulations were performed, each characterized by a single α and h^* (see Table 6). Figs. 17–21 reports the geometrical wake parameters L_f, W_v, a, b, L_b for selected experiments, alongside the reference PSSs and PODA results. The following considerations are derived:

- $\alpha = 0$: With no variation in porous properties, the recirculating wake shrinks as h^* increases. A coarse grid does not properly capture the physics in the transition zone, and the model perceives a sharp discontinuity of the porous medium properties. Discrepancies from the reference grow with Re, reflecting under-resolved velocity and pressure gradients. Stronger local gradients at higher Re amplify numerical diffusion on coarse grids, consistent with trends observed for solid cylinder in Section 4.1. Physically, the interface behaves as a high-resistance barrier, limiting momentum transfer into the porous region and producing stronger viscous dissipation.

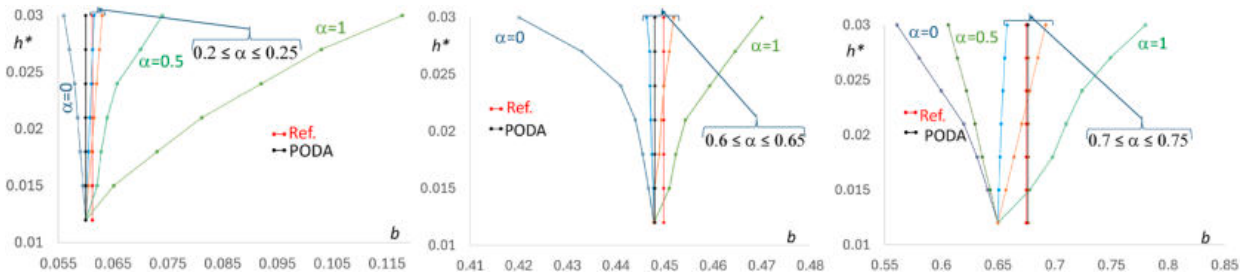

Fig. 18. Computed (dimensionless) b vs. h^*. From left to right, $Re = 10$, $Re = 25$, $Re = 40$, M1.

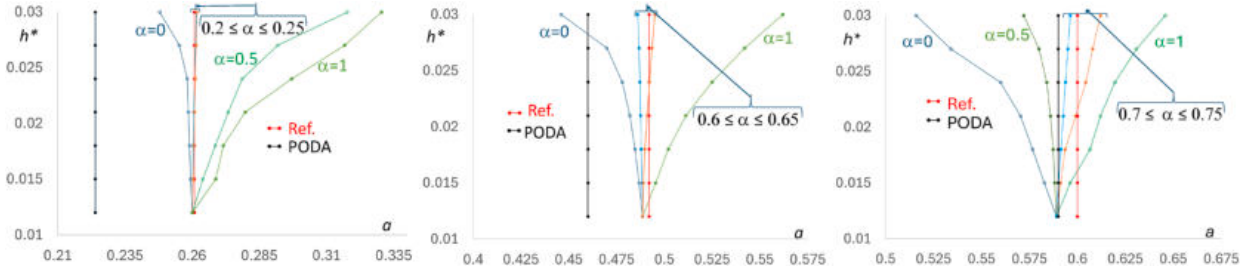

Fig. 19. Computed (dimensionless) a vs. h^*. From left to right, $Re = 10$, $Re = 25$, $Re = 40$, M1.

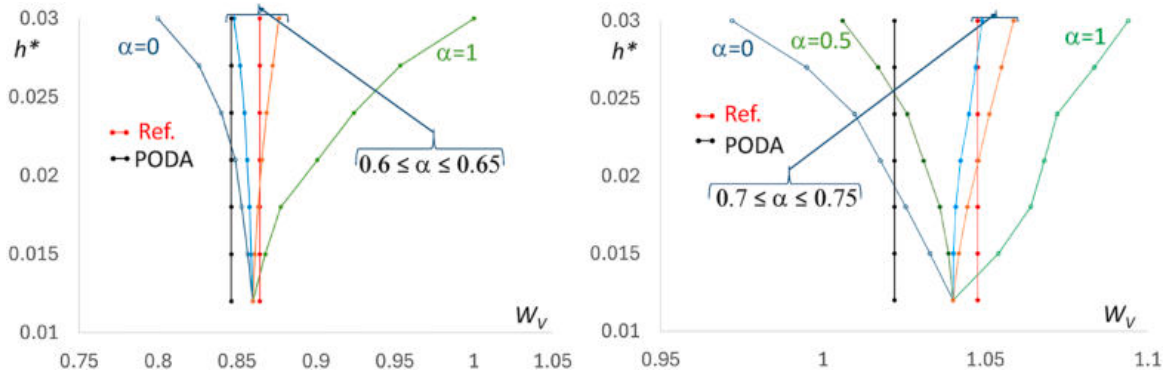

Fig. 20. Computed (dimensionless) W_V vs. h^*. $Re = 25$ (left), $Re = 40$ (right), M1.

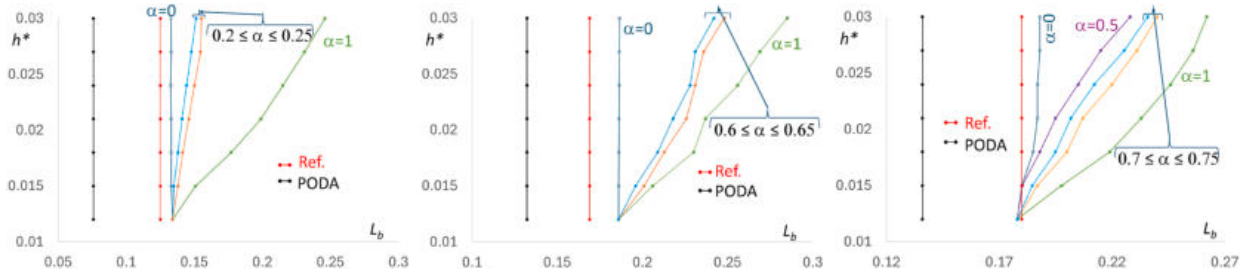

Fig. 21. Computed (dimensionless) L_b vs. h^*. From left to right, $Re = 10$, $Re = 25$, $Re = 40$, M1.

- $\alpha = 1$: Incorporating the change in porous material properties, the physics of the fluid-porous interface dominates the downstream flow. The recirculating wake increases in size with h^*, highlighting that the interfacial resistance profile primarily governs wake development, with grid resolution playing a secondary role.
- Streamwise penetration (L_b): Grid size effects are minor; the wake penetration is largely determined by $\mathcal{P}_n^{\alpha,*}$. For $\alpha = 0$, MSODA matches the reference, particularly at low Re. Increasing α smooths the profile, reducing effective resistance and allowing deeper penetration from the rear side. Flow within the porous medium is nearly orthogonal to the interface, with minimal vortical activity, explaining the low sensitivity to grid resolution.

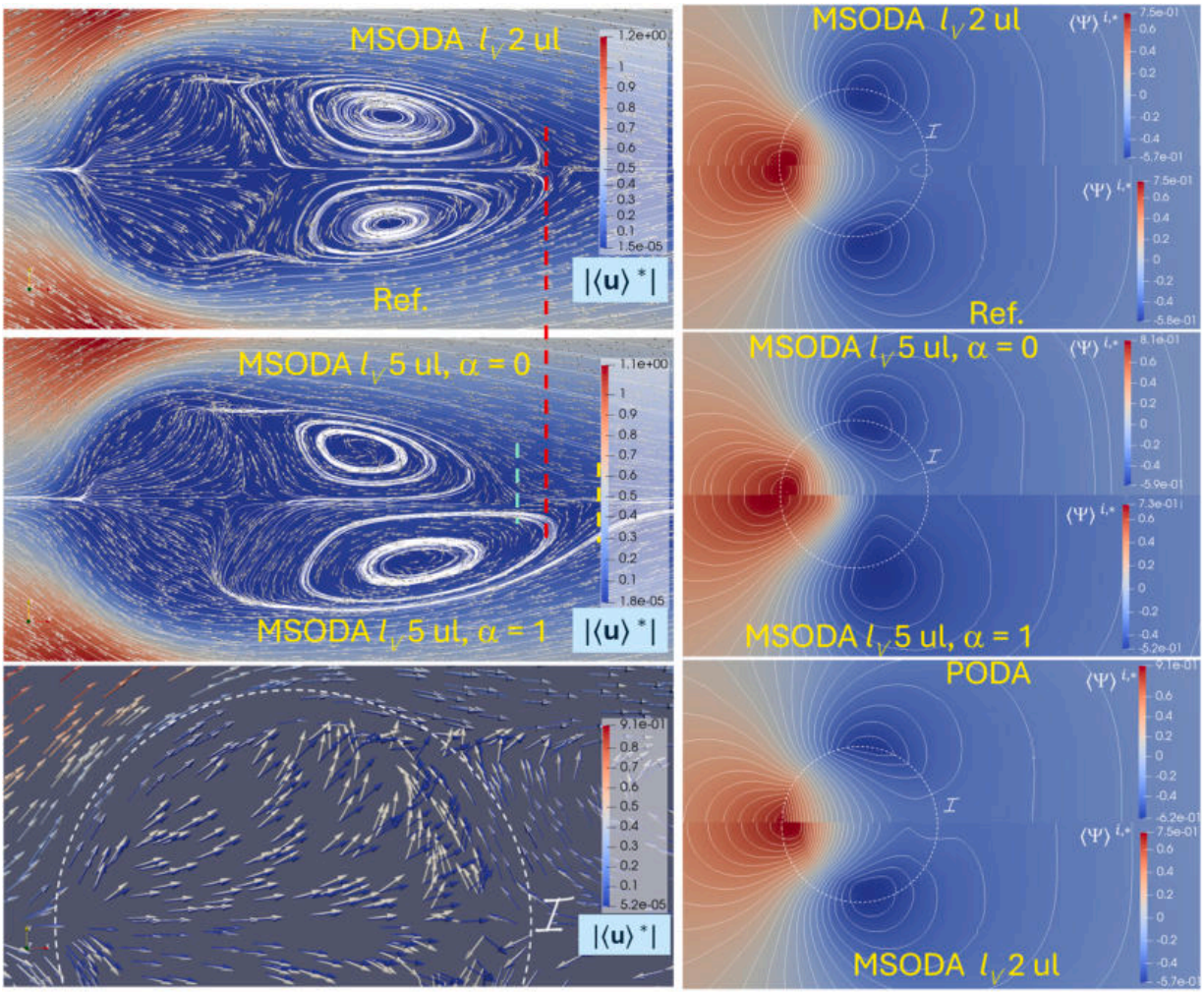

(a) Computed MSODA $\langle \mathbf{u} \rangle$ vs. reference solution. Top row: computed MSODA solution assuming the profile $P_{\tilde{n}}^{\alpha,*}$ vs the reference filtered solution. Central row : computed MSODA solution assuming the profiles $P_5^{1,*}$ and $P_5^{0,*}$. The dotted lines mark the downstream extent of the vortex. Bottom row, comparison of the velocity fields close to the downstream boundary of the cylinder; white arrows, solution of the MSODA solver, blue arrows, reference (filtered) solution.

(b) Comparison among the reference (filtered) pressure field, the pressure field provided by the MSODA in the same scenarios as in Fig. 22a and the PODA pressure field.

Fig. 22. Velocity and pressure fields, M1, $Re = 25$.

- PODA results follow similar trends, confirming that a sharp interface limits momentum transfer, enhancing viscous dissipation and underestimating the wake extent.
- W_v for $Re = 10$ is omitted due to attached downstream vortices, complicating measurement.

These trends were consistent across materials M2 and M3 (not shown).

Fig. 22(a) compares MSODA velocity fields for M1 at $Re = 25$ with the reference. Only half the domain is shown due to symmetry. Using $\mathcal{P}_{\tilde{n}}^{*}$ yields good agreement (top row), while some discrepancies appear near the downstream boundary (bottom row). Profiles with $n = 5ul$ and $\alpha = 0, 1$ (central row) under- or overpredict the downstream wake, respectively, consistent with the effects of interfacial resistance on momentum transfer and energy dissipation. Fig. 22(b) reports the corresponding kinematic pressure fields $\langle \Psi \rangle^{i,*}$. Steeper profiles (PODA or MSODA with $\mathcal{P}_n^{\alpha,*}$, $n > \tilde{n}$, $\alpha = 0$) restrict momentum transfer, forcing abrupt flow deviation, which increases local stagnation pressure. Pressure minima at $\theta \simeq \pi/4$ and $3\pi/4$ coincide with flow acceleration zones around the cylinder. Smoother profiles ($\alpha = 1$) allow gradual penetration into the porous interface, reducing resistance, preserving momentum, and producing a larger, more extended downstream wake.

Numerical experiments conducted on materials M1, M2, and M3 demonstrate that the MSODA solution employing the $\mathcal{P}_{\tilde{n}}^{*}$ profile consistently reproduces the reference averaged PSSs solution, particularly for the geometric parameters L_f, a, b, W_v. For larger REV

Table 7
The ranges of α_{opt} vs Re for materials M1, M2 and M3.

Re	α_{opt} Range
10	$\in [\simeq 0.200, \simeq 0.250]$
15	$\in [\simeq 0.400, \simeq 0.425]$
20	$\in [\simeq 0.520, \simeq 0.550]$
25	$\in [\simeq 0.600, \simeq 0.650]$
30	$\in [\simeq 0.650, \simeq 0.675]$
35	$\in [\simeq 0.675, \simeq 0.725]$
40	$\in [\simeq 0.700, \simeq 0.750]$

Table 8
$E_{\text{MSODA},q}$ with $\alpha = \alpha_{opt}$ vs Re, materials M1, M2 and M3.

Re	E_{MSODA,L_f}	$E_{\text{MSODA},b}$	$E_{\text{MSODA},a}$	E_{MSODA,W_V}	E_{MSODA,L_b}	$E_{\text{MSODA},L_b}(\alpha = 0)$
10	$\simeq 3.40 \cdot 10^{-3}$	$\simeq 2.50 \cdot 10^{-3}$	$\simeq 3.70 \cdot 10^{-3}$	$\simeq 3.80 \cdot 10^{-3}$	$[\simeq 0.21, \simeq 0.24]$	$\simeq 7.00 \cdot 10^{-2}$
15	$\simeq 4.30 \cdot 10^{-3}$	$\simeq 3.20 \cdot 10^{-3}$	$\simeq 4.50 \cdot 10^{-3}$	$\simeq 4.30 \cdot 10^{-3}$	$[\simeq 0.27, \simeq 0.31]$	$\simeq 1.20 \cdot 10^{-1}$
20	$\simeq 5.00 \cdot 10^{-3}$	$\simeq 3.80 \cdot 10^{-3}$	$\simeq 5.90 \cdot 10^{-3}$	$\simeq 6.10 \cdot 10^{-3}$	$[\simeq 0.32, \simeq 0.37]$	$\simeq 1.07 \cdot 10^{-1}$
25	$\simeq 5.80 \cdot 10^{-3}$	$\simeq 4.20 \cdot 10^{-3}$	$\simeq 7.20 \cdot 10^{-3}$	$\simeq 7.60 \cdot 10^{-3}$	$[\simeq 0.43, \simeq 0.46]$	$\simeq 1.00 \cdot 10^{-1}$
30	$\simeq 6.75 \cdot 10^{-3}$	$\simeq 6.30 \cdot 10^{-3}$	$\simeq 1.10 \cdot 10^{-2}$	$\simeq 1.15 \cdot 10^{-2}$	$[\simeq 0.25, \simeq 0.32]$	$\simeq 7.50 \cdot 10^{-2}$
35	$\simeq 9.00 \cdot 10^{-3}$	$\simeq 1.10 \cdot 10^{-2}$	$\simeq 1.30 \cdot 10^{-2}$	$\simeq 1.32 \cdot 10^{-2}$	$[\simeq 0.15, \simeq 0.23]$	$\simeq 5.80 \cdot 10^{-2}$
40	$\simeq 1.45 \cdot 10^{-2}$	$\simeq 1.75 \cdot 10^{-2}$	$\simeq 1.50 \cdot 10^{-2}$	$\simeq 1.60 \cdot 10^{-2}$	$[\simeq 0.13, \simeq 0.20]$	$\simeq 4.00 \cdot 10^{-2}$

sizes $l_{\mathcal{V}} = nul$ with $n > \tilde{n}$, our previous analysis indicates the existence of an optimal range of α, denoted as α_{opt}, for which the profile $\mathcal{P}_n^{\alpha_{opt},*}$ minimizes the discrepancies between the MSODA results and the reference solution. The optimal α_{opt} was found to be Reynolds-number dependent, as summarized in Table 7, and is remarkably consistent across all three porous media. As Re increases, α_{opt} shifts toward higher values (the orange and cyan curves in Figs. 17 to 20, associated to the values of α in the optimal range, show the best agreement with the reference solution). This confirms that minimizing the numerical error at higher Re requires progressively smoother $\mathcal{P}_n^{\alpha,*}$ profiles, effectively emulating a lower flow resistance within the porous cylinder.

The dependence of α_{opt} on the Reynolds number reflects the underlying physics of momentum exchange across the fluid-porous interface. As Re increases, inertial forces become dominant, leading to steeper pressure gradients and a more pronounced stagnation effect on the upstream face of the cylinder. In this context, α_{opt} effectively regulates the "receptivity" of the porous medium to external momentum: a larger α_{opt} provides a smoother transition that prevents numerical overshoots of the pressure gradient at the interface.

This behavior, despite neglecting pore-scale inertial effects in the reference PSS, is not a contradiction but a macro-scale hydrodynamic requirement. While the microscopic flow within the porous medium remains in the linear Stokes regime, the macroscopic field around the cylinder is dominated by inertia. Consequently, α_{opt} does not need to compensate for material-specific non-linearities, such as Forchheimer effects; instead, it reflects the macroscopic flow redistribution and the dynamic pressure gradients at the interface. Although a formal functional relationship between α_{opt} and Re is not explicitly derived, the observed trend remains remarkably consistent across the investigated microstructures.

As previously discussed, increasing Re from 10 to 40 amplifies the numerical error associated with grid resolution. This is evident in Figs. 17 to 20, where the deviation between the MSODA solution using $\mathcal{P}_n^{\alpha_{opt},*}$ and the reference solution increases with Re.

To quantify the relative accuracy of MSODA and PODA, we define the relative error of a geometrical parameter $q = L_f, a, b, W_v, L_b$ as

$$E_{s,q} = \frac{\|q_s - q_{ref}\|}{q_{ref}},$$

where s = MSODA or PODA, q_s is the value computed by the solver, and q_{ref} is the value from the filtered PSSs reference solution. Table 8 reports $E_{MSODA,q}$ for $\mathcal{P}_n^{\alpha_{opt},*}$ as a function of Re, along with E_{MSODA,L_b} for $\alpha = 0$. Table 9 summarizes the error ranges for MSODA ($\alpha = 0, 1, \alpha_{opt}$) and PODA across $10 \leq Re \leq 40$. The first and second entries correspond to $Re = 10$ and $Re = 40$, respectively. Consistent with Figs. 17 to 20, $E_{MSODA,q}$ for $q = L_f, a, b, W_v$ increases with Re for $\alpha = 0$, while decreasing for $\alpha = 1$. At low Re, errors for α_{opt} are one to two orders of magnitude smaller than those for $\alpha = 0$ or 1; at higher Re, they scale approximately as $[0.1, 0.25] \times E_q$. The peak errors E_{MSODA,L_b} occur at $Re \simeq 20 - 25$, corresponding to the non-monotonic trend of L_b in Fig. 14, left, resulting from the interplay between upstream-oriented recirculating flow and the downstream-oriented base flow. The ratio of E_{MSODA,L_b} between $\alpha = 0$ and α_{opt} remains within $[0.2, 0.33]$, while MSODA errors for α_{opt} range from $\simeq 0.01 \times E_{PODA,q}$ to $\simeq 0.1 \times E_{PODA,q}$ as Re increases from 10 to 40.

Figs. 23–27 show the velocity components $\langle u_x \rangle^*$ and $\langle u_y \rangle^*$, and the kinematic pressure $\langle \Psi \rangle^{i,*}$, along the four lines defined in Fig. 8(b). MSODA results obtained with $\mathcal{P}_{\tilde{n}}^*$ and $\mathcal{P}_n^{\alpha_{opt},*}$ show excellent agreement with the reference. For brevity, results are presented for three REV sizes: $l_{\mathcal{V}} = 2ul, 3.5ul, 5ul$.

Smoother profiles ($\alpha > \alpha_{opt}$) produce higher absolute velocities within the porous cylinder compared to the reference, due to reduced flow resistance, enhanced momentum transfer, and increased kinetic energy across the interface (Section 4.2.1). Conversely, $\alpha < \alpha_{opt}$ increases the simulated resistance, reducing momentum transfer and kinetic energy, resulting in underprediction of velocity

Table 9
Ranges of $E_{s,q}$ for $10 \leq Re \leq 40$, materials M1, M2 and M3.

q	$E_{\text{MSODA},q}$ $(\alpha = 0)$	$E_{\text{MSODA},q}$ $(\alpha = 1)$	$E_{\text{MSODA},q}$ $(\alpha = \alpha_{\text{opt}})$	$E_{\text{PODA},q}$
L_f	$[\simeq 0.026, \simeq 0.112]$	$[\simeq 0.080, \simeq 0.270]$	$[\simeq 3.4, \simeq 14.5] \cdot 10^{-3}$	$[\simeq 0.030, \simeq 0.051]$
a	$[\simeq 0.050, \simeq 0.140]$	$[\simeq 0.050, \simeq 0.400]$	$[\simeq 3.7, \simeq 15.0] \cdot 10^{-3}$	$[\simeq 0.059, \simeq 0.073]$
b	$[\simeq 0.010, \simeq 0.100]$	$[\simeq 0.089, \simeq 0.190]$	$[\simeq 2.5, \simeq 17.5] \cdot 10^{-3}$	$[\simeq 0.022, \simeq 0.043]$
W_V	$[\simeq 0.053, \simeq 0.162]$	$[\simeq 0.056, \simeq 0.387]$	$[\simeq 3.8, \simeq 16.0] \cdot 10^{-3}$	$[\simeq 0.062, \simeq 0.089]$
L_b	see Table 8	$[\simeq 0.450, \simeq 0.960]$	see Table 8	$[\simeq 0.310, \simeq 0.740]$

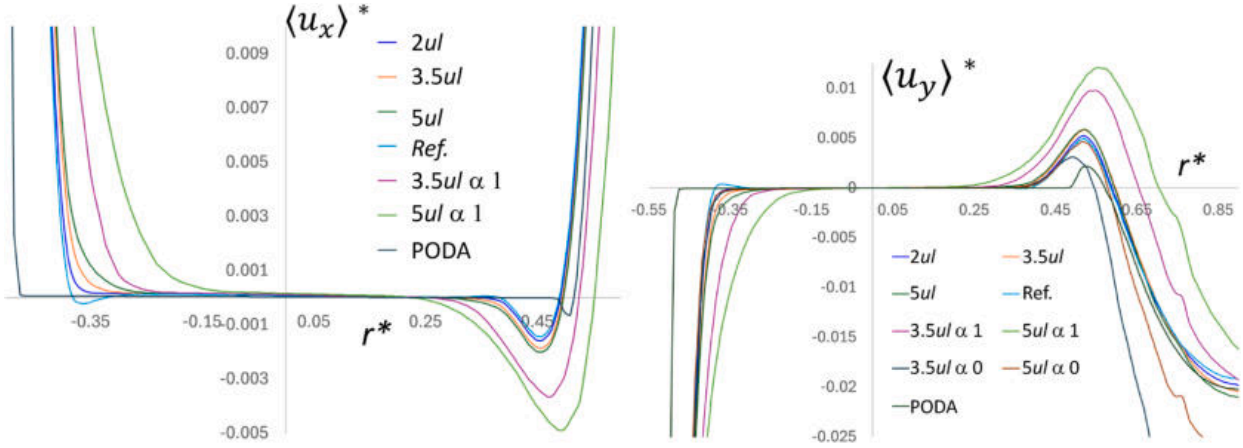

Fig. 23. Computed $\langle u_x \rangle^*$ (left) and $\langle u_y \rangle^*$ (right) along line 1 shown in Fig. 8(b), $Re = 25$, M1. Zoom near the interface $\mathcal{I}$. If α is not specified in the MSODA results, it means $\alpha = \alpha_{opt}$, and the same applies for Figs. 24 to 27.

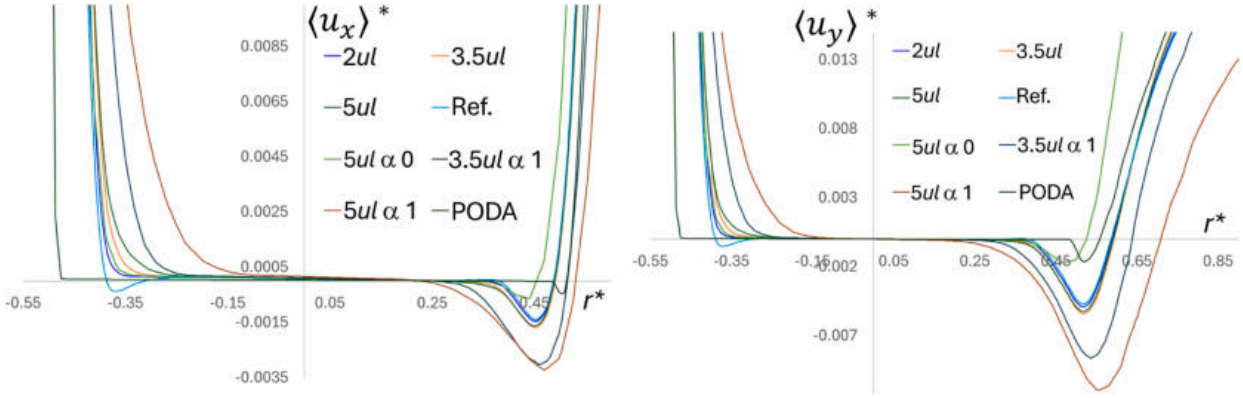

Fig. 24. Computed $\langle u_x \rangle^*$ (left), and $\langle u_y \rangle^*$ (right) along line 2 shown in Fig. 8(b), $Re = 25$, M1. Zoom near the interface $\mathcal{I}$.

components near the interface. The PODA solver exhibits the same trend, with a larger magnitude of deviation. Notably, MSODA with $\alpha = 0$ accurately predicts $\langle u_x \rangle^*$ along line 4, particularly near $r^* \simeq 0.4$, consistent with the observed inner vortex front L_b and flow penetration.

Compared to the reference and MSODA solutions with $\mathcal{P}^*_{\tilde{n}}$ and $\mathcal{P}^{\alpha_{opt},*}_n$, cases with $\alpha > \alpha_{opt}$ underpredict local $\langle \Psi \rangle^{i,*}$ minima along line 3 ($r^* \simeq \pm 0.5$) and the local maxima along line 4 ($r^* \simeq 0.5$). Conversely, higher-resistance scenarios ($\alpha < \alpha_{opt}$ or PODA) overpredict these local extrema. These trends corroborate the physical interpretation of momentum transfer and flow resistance at the fluid-porous interface discussed in Fig. 22(b).

The force acting on the porous cylinder has been computed by integrating Eq. (6) over the cylinder cross-section $A_{cyl} = \pi D^2/4$. Its dimensionless form reads

$$\mathbf{F}^*_c = \int_{A^*_{cyl}} \mathbf{f}^* \, d\sigma = \int_0^{2\pi} \int_0^{R^*} \mathbf{f}^* \, dr^* d\theta, \qquad \mathbf{f}^* = \frac{\phi(r^*)}{Re\, Da(r^*)} \mathbf{u}^*,$$

where $A^*_{cyl} = \pi R^{*2} = \pi/4$ is the dimensionless cylinder cross-section, $R^* = 0.5$ is the dimensionless cylinder radius, and $r^* = d^* + R^*$, as specified in Section 4.2.1.

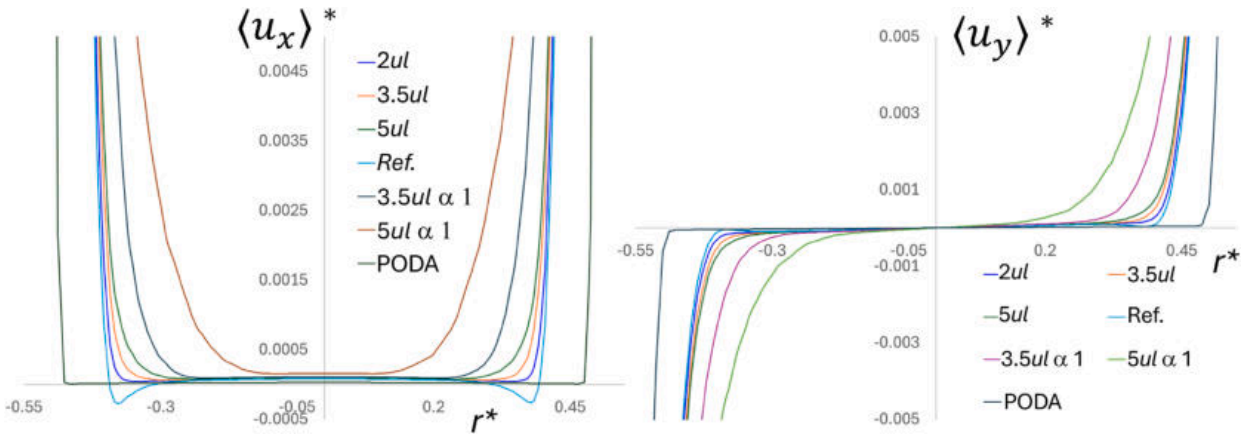

Fig. 25. Computed $\langle u_x \rangle^*$ (left), and $\langle u_y \rangle^*$ (right) along line 3 shown in Fig. 8(b), $Re = 25$, M1. Zoom near the interface $\mathcal{I}$.

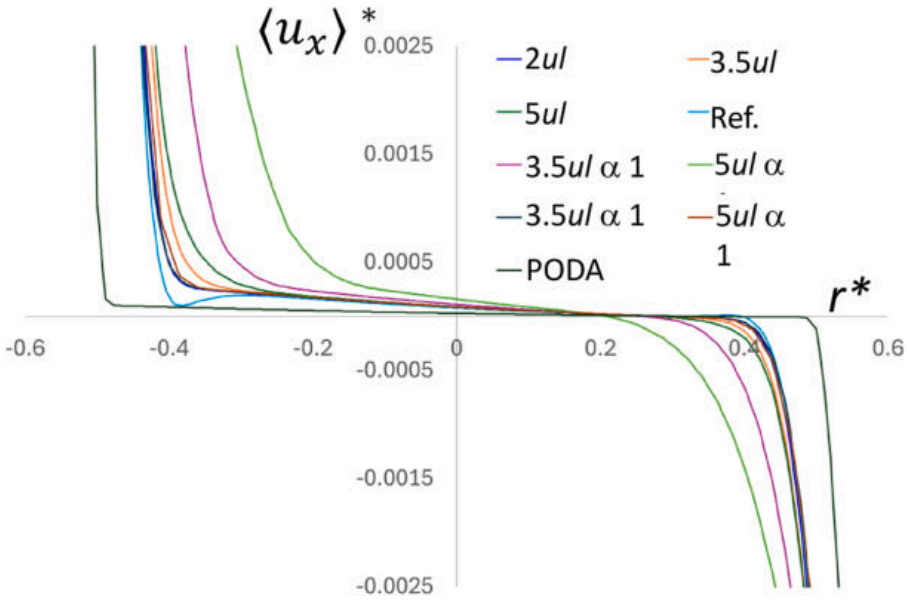

Fig. 26. Computed $\langle u_x \rangle^*$ along line 4 shown in Fig. 8(b), $Re = 25$, M1. Zoom close to the interface $\mathcal{I}$.

In Fig. 28, we show the x-component of $\mathbf{F}_c^*$, i.e., the drag force F_D^*, for various Reynolds numbers, computed by the MSODA solver with profiles $\mathcal{P}_n^{\alpha,*}$ ($0 \le \alpha \le 1$, $2ul \le l_{\mathcal{V}} \le 5ul$). The figure also reports F_D^* from the PODA solver and the reference solution (the x-component of the dimensionless integral of Eq. (5) over A_{cyl}^*). Forces in the y-direction are negligible, being three to four orders of magnitude smaller.

Key observations from Fig. 28 are:

- The drag force computed with MSODA using $\mathcal{P}_{\tilde{n}}^*$ profiles agrees quite well with the reference solution.
- For $\mathcal{P}_n^*$ with $n > \tilde{n}$, the best match is obtained using $\mathcal{P}_n^{\alpha_{opt},*}$ (curves in orange and green correspond to α_{opt} values in Table 7).
- MSODA overestimates the drag for $\alpha < \alpha_{opt}$ and underestimates it for $\alpha > \alpha_{opt}$. The PODA solver predicts F_D^* approximately 1.65–2.85 times higher. Physically, as discussed in Figs. 22 and 23 to 27, increasing the flow resistance across the interface $\mathcal{I}$ reduces momentum transfer into the cylinder. Reduced filtration capacity results in higher positive pressure at the upstream stagnation point and larger negative pressure downstream ($\theta \simeq 0$), increasing the drag. Moreover, steeper velocity gradients near the interface enhance local shear stress, further contributing to the drag. The opposite occurs when the flow resistance decreases.
- These effects are confirmed in Fig. 29, where the spatial distribution of $\mathbf{f}^*$ is shown for $Re = 25$ with $\mathcal{P}_{\tilde{n}}^*$ (left) and the difference between penalized and MSODA solutions (right). As expected, the largest differences occur near $\mathcal{I}$.

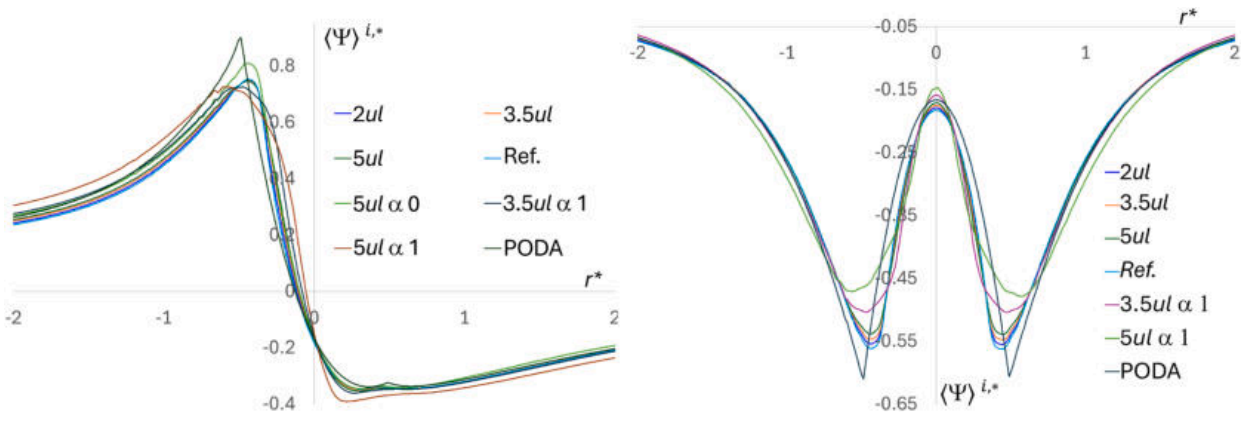

Fig. 27. Computed $\langle\Psi\rangle^{i,*}$, along left) line 4, center) line 3, right) line 1 (lines shown in Fig. 8(b)).

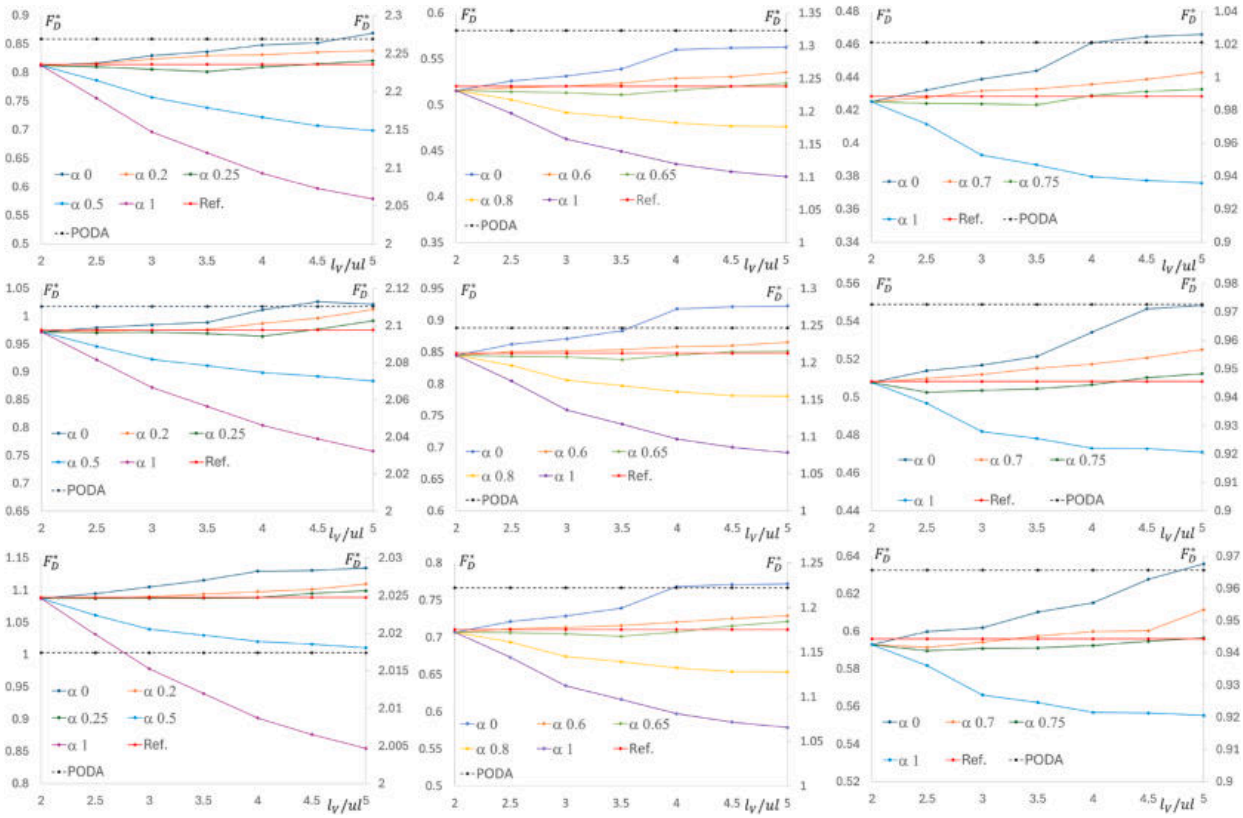

Fig. 28. Computed (dimensionless) forces F_D^* on the porous cylinder vs. l_V, $0 \le \alpha \le 1$. Top row, M1, central row, M2, bottom row, M3. Left) $Re = 10$, center) $Re = 25$, right) $Re = 40$. Nomenclature: "α s" - solution of the MSODA solver assuming the profile $\mathcal{P}_n^{\alpha,*}$ with $\alpha = s$. Values of the PODA solver on the secondary axis.

The relative error of the drag force with respect to the reference is defined as

$$E_{F_D^*} = \frac{\|F^*_{D,MSODA} - F^*_{D,ref}\|}{F^*_{D,ref}}.$$

Using $\mathcal{P}_n^{\alpha_{opt},*}$, the largest errors, associated with the largest REV size, are $E_{F_D^*} \in [\simeq 1\times10^{-3}, \simeq 3\times10^{-3}]$ for $10 \le Re \le 40$. Using $\alpha = 0$ or $\alpha = 1$, the corresponding errors reach $E_{F_D^*} \simeq 0.12$ and $E_{F_D^*} \simeq 0.28$, respectively.

In Fig. 30, we plot $\int_0^{R^*} \mathbf{f}^* dr^*$ as a function of $\theta \in [0, 2\pi]$, computed with MSODA ($\mathcal{P}_n^{\alpha,*}$), PODA, and the reference. The local maxima and minima correlate with maxima ($\theta \simeq 0.7\pi, 1.4\pi$) and minima ($\theta \simeq 0, \pi$) of u_x^*, respectively. At $Re = 40$, PODA overpredicts the drag

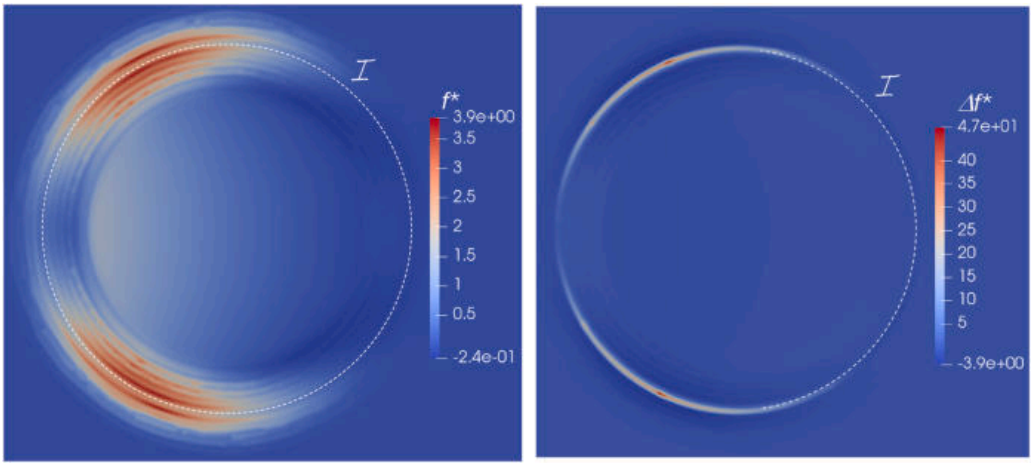

Fig. 29. Left) $\mathbf{f}^*$ computed by the MSODA, $l_v = 2ul$. Right) $\Delta\mathbf{f}^*$ difference between $\mathbf{f}^*$ computed by the PODA and the MSODA. $Re = 25$, M1.

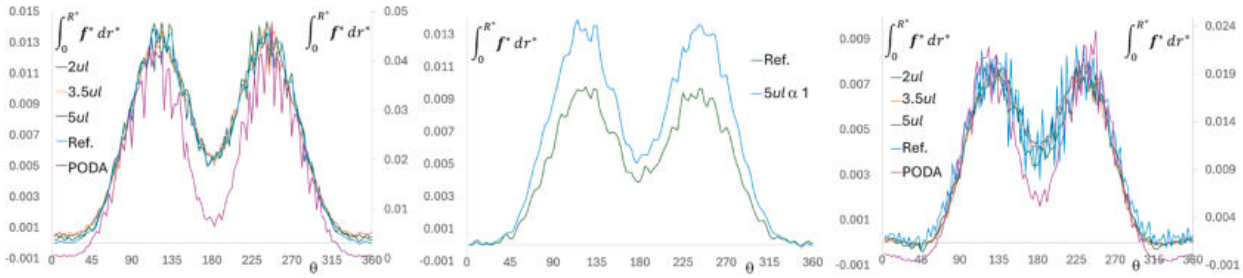

Fig. 30. Computed $\int_0^{R^*} \mathbf{f}^* dr^*$, M1. Left) $Re = 10$, MSODA solution with $\alpha = \alpha_{opt}$ vs PODA solution, center) $Re = 10$, MSODA solution with $\alpha > \alpha_{opt}$, right) $Re = 40$, MSODA solution with $\alpha = \alpha_{opt}$ vs PODA solution. PODA solution values on the secondary axis.

at the stagnation point ($\theta = \pi$) and underpredicts it downstream ($\theta = 0$), consistent with previously noted overestimation of positive pressure and underestimation of negative pressure (Fig. 27, left).

Overall, MSODA with $\mathcal{P}_n^{\alpha_{opt},*}$ reproduces the reference drag accurately. If $\alpha > \alpha_{opt}$, drag is underestimated, reflecting underpredicted flow resistance within the porous medium.

5. Conclusions

In this study, the interaction between a circular porous cylinder and a steady, unconfined flow was investigated using a Mesoscopic One-Domain Approach (MSODA). By deriving porosity and permeability profiles from filtered PSSs, we performed a detailed analysis of the flow field, wake structure, and drag forces.

The key conclusions of this work are summarized as follows:

- **Interface physics and momentum transfer:** Comparison with the reference solution demonstrates that MSODA successfully captures the continuous transition of hydraulic properties across the fluid-porous interface. Unlike traditional "penalized" (PODA) approaches, which impose a sharp discontinuity, the proposed method allows for realistic momentum transfer, preventing the overestimation of drag forces and the underestimation of flow penetration.
- **Anisotropy and surface alignment:** Aligning the principal directions of the permeability tensor with the tangential and normal directions of the cylinder surface (curvilinear framework) significantly improves model accuracy. This alignment correctly captures tangential viscous shear and pressure-driven filtration, whereas standard Cartesian alignment introduces unphysical resistance (see Appendix C).
- **Spatial shift of the permeability profiles:** PSS-informed data show a distinct spatial shift between the porosity and the resistance ($\mathfrak{K}$) profiles, with the latter being displaced toward the inner porous domain. This shift reflects the gradual development of the viscous drag: near the interface, the flow is less constrained by the solid microstructure, leading to a localized reduction in $\mathfrak{K}$ compared to the bulk porous core. This displacement ensures that the momentum transition is correctly captured, preventing the unphysical drag overestimation typical of sharp-interface models.
- **Sensitivity to REV scaling:** Although the model bypasses the mathematical complexity of non-local weighting functions in Eq. (4), it recovers the essential physics of the transition layer. The minimal deviations observed with respect to the reference solutions (especially when adopting an optimized scaling parameter α_{opt} or a small REV size) demonstrate that the proposed local closure

is sufficient for engineering applications involving complex porous-fluid interactions. The choice of Representative Elementary Volume (REV) size for filtering dictates the smoothness of the transition zone. The smallest REV provides the best match with reference PSS data, while larger REV sizes act as a "hydrodynamic buffer," increasing momentum transfer across the interface and flow kinetic energy, reducing velocity gradients, overpredicting the recirculating wake, and underestimating the drag force.

- **Sensitivity of the Transition Parameter α:** The analysis of the optimal transition parameter, α_{opt}, reveals a clear trend: while it is strictly dependent on the Reynolds number, it remains remarkably consistent across all the different porous microstructures investigated. This suggests that α_{opt} is governed by the macro-scale flow regime rather than the specific geometry of the solid inclusions. Although a formal universal law is not explicitly derived, this finding provides a robust heuristic for calibrating mesoscopic models across various porous media without requiring case-specific pore-scale iterations.

Thanks to the scalability of the porosity and permeability profiles, the preliminary PSSs constitute a "one-time effort" confined to limited representative domains. Unlike closure techniques based on the Volume Averaging Method, Generalized Transport Equations, or homogenization–which require assumptions of periodicity and/or scale separation–the present approach leverages PSSs to directly capture mesoscopic heterogeneity. This data-driven methodology allows treatment of transition zones and provides a robust, scalable framework for large-scale applications. Classical theoretical approaches, in contrast, often involve added complexity that may outweigh their practical advantages.

These findings have important implications for applications where accurate interface modeling is critical. For example, in passive flow control, porous coatings suppress vortex-induced vibrations in engineering structures. In biomedical engineering, interactions between blood flow and porous scaffolds require precise shear stress calculations at the interface to ensure cell viability. Moreover, the method is relevant for industrial filtration and environmental hydrodynamics (e.g., flow through vegetation), where penetration depth and wake structure directly affect system efficiency. MSODA's ability to accurately predict drag and shear stresses represents a significant advantage over conventional penalized methods.

The limitations of the present study include:

- **Steady-state constraint:** The analysis is restricted to steady, low-Reynolds-number flows.
- **Rigid matrix assumption:** The porous medium is assumed to be composed of rigid, fixed solid inclusions. This neglects poroelastic deformations or fluid-structure interactions that may occur in soft scaffolds or under high-pressure gradients.
- **Negligible internal inertia:** The model assumes negligible inertial effects (Forchheimer terms) within the porous cylinder, which is valid only for low-permeability media and low-velocity regimes.

Recommended extensions and future research directions:

- **Unsteady and inertial regimes:** Future studies should assess MSODA performance in unsteady flows with non-negligible inertial effects within the porous medium.
- **3D complex geometries:** Extending the mesoscopic approach to 3D complex geometries, such as biological scaffolds or irregular environmental filters, is recommended to validate the robustness of tangential-orthogonal permeability alignment in non-circular domains.

CRediT authorship contribution statement

Costanza Aricò: Writing – original draft, Visualization, Validation, Software, Resources, Methodology, Investigation, Formal analysis, Data curation, Conceptualization, Supervision, Writing – review & editing; **Rainer Helmig:** Supervision, Resources, Project administration, Funding acquisition; **Martin Schneider:** Supervision, Resources, Project administration, Methodology, Investigation, Funding acquisition, Conceptualization.

Data availability

Data will be made available on request.

Declaration of competing interest

The authors declare that they have no known competing financial interests or personal relationships that could have appeared to influence the work reported in this paper.

Acknowledgment

This work was supported by the German Research Foundation (DFG), by funding Sonderforschungsbereich (SFB) 1313 (Project Number 327154368, Research Project A02), University of Stuttgart, and by funding SimTech via Germany's Excellence Strategy (EXC 2075–390740016), University of Stuttgart.

Appendix A. List of main symbols and acronyms

Symbol / Acronym	Description
Symbols	
Φ^*, Φ_0	any dimensionless variable Φ and its bulk value
$\langle\Phi\rangle$, $\langle\Phi\rangle^i$	surface and intrinsic average values of Φ
$\Psi = \frac{p}{\rho}$	Kinematic pressure
Re, Re_p	Macroscopic and pore-scale Reynolds numbers
D	Diameter of the porous cylinder
$\mathcal{I}, d, d^*$	Idealized cylinder interface, distance from $\mathcal{I}$
ϕ, $\mathbf{K}$, $\mathfrak{K}$	Porosity, permeability tensor and its inverse $\mathbf{K}^{-1}$
$\mathbf{n}, \tau$	Unit vectors orthogonal and tangential to the interface
$\mathcal{V}, S$	Averaging volume and interface between phases
$l_\mathcal{V}, n, \tilde{n}$	REV size ($l_\mathcal{V} = n \cdot ul$), multiplier n
Da, Da_0	Position-dependent and bulk Darcy numbers (K/D^2)
D_n, $\mathcal{D}_n^*$, $\tilde{\mathcal{D}}^*$	Physical and dimensionless extent of transition zone
α, α_{opt}	Shape parameter and its optimal value
$\mathcal{P}_n^*$, $\mathcal{P}_n^{\alpha,*}$	Dimensionless profile of the resistive term
h, h^*	Grid size and its dimensionless value
Acronyms	
REV, PSS	Representative Elementary Volume and Pore-Scale Simulation
ODA, MSODA	One-Domain-Approach and Mesoscopic One-Domain-Approach
PODA, TDA	Penalized ODA (macroscopic) and Two-Domain-Approach
SI	Solid Inclusion

Appendix B. Considerations for the $\mathbf{F}_d$ term in Eq. (5) and its closure

Following [32], the average value of the term $\nabla\Psi$ in the momentum Eq. (1a) can be written as

$$\langle\nabla\Psi\rangle = \nabla\langle\Psi\rangle + \int_S G(\Psi\mathbf{n})ds = \nabla\left(\phi\langle\Psi\rangle^i\right) + \int_S G(\Psi\mathbf{n})ds = \phi\nabla\langle\Psi\rangle^i + \langle\Psi\rangle^i\nabla\phi + \int_S G(\Psi\mathbf{n})ds, \tag{B.1}$$

where we have omitted the subscript $\mathbf{x}$ in the surface average values for the sake of simplicity. Applying the averaging theorem to the viscous term of the momentum Eq. (1a), we get [32],

$$\nu\langle\nabla^2\mathbf{u}\rangle = \nu\nabla\cdot\langle\nabla\mathbf{u}\rangle + \nu\int_S G(\nabla\mathbf{u}\ \mathbf{n})ds = \nu\nabla^2\langle\mathbf{u}\rangle + \nu\int_S G(\nabla\mathbf{u}\ \mathbf{n})ds. \tag{B.2}$$

So far, no length scale constraint has been imposed in Eqs. (B.1) and (B.2).

Setting $\Phi = 1$ in Section 2, it is easy to obtain (e.g., [32]),

$$-\nabla\phi = \int_S G\mathbf{n}ds. \tag{B.3}$$

Introducing now the scale constraint $l_\mathcal{V} << L$, making use of the Gray's decomposition [31] for the instantaneous values of the kinematic pressure Ψ and velocity $\mathbf{u}$,

$$\Psi = \langle\Psi\rangle^i + \tilde{\Psi}, \qquad \mathbf{u} = \langle\mathbf{u}\rangle^i + \tilde{\mathbf{u}}, \tag{B.4}$$

with $\tilde{\Psi}$ and $\tilde{\mathbf{u}}$ the deviations from the intrinsic average values $\langle\Psi\rangle^i$ and $\langle\mathbf{u}\rangle^i$, and thanks to Eq. (B.3), Eqs. (B.1), B.2 become respectively (e.g., [32])

$$\phi\nabla\langle\Psi\rangle^i + \langle\Psi\rangle^i\nabla\phi + \int_S G(\Psi\mathbf{n})ds = \phi\nabla\langle\Psi\rangle^i - \langle\Psi\rangle^i\int_S G\mathbf{n}ds + \int_S G(\Psi\mathbf{n})ds = \phi\nabla\langle\Psi\rangle^i + \int_S G\left(\tilde{\Psi}\mathbf{n}\right)ds, \tag{B.5}$$

and

$$\nu\nabla^2\langle\mathbf{u}\rangle + \nu\int_S G(\nabla\mathbf{u}\ \mathbf{n})ds = \nu\nabla^2\langle\mathbf{u}\rangle + \nu\nabla\langle\mathbf{u}\rangle^i\int_S G\ \mathbf{n}ds + \nu\int_S G(\nabla\tilde{\mathbf{u}}\ \mathbf{n})ds = \nu\nabla^2\langle\mathbf{u}\rangle - \nu\nabla\phi\nabla\langle\mathbf{u}\rangle^i + \nu\int_S G(\nabla\tilde{\mathbf{u}}\ \mathbf{n})ds. \tag{B.6}$$

Due to the scale constraint, $\langle\Psi\rangle^i$ and $\langle\mathbf{u}\rangle^i$ can be assumed constant with respect to the integral over S in Eqs. (B.5) and B.6, and after simple manipulations Eq. (5) becomes (e.g., [32] and references therein),

$$\mathbf{F}_d = -\langle\Psi\rangle^i \nabla\phi - \int_S (G(-\Psi\mathbf{I} + \nu\nabla\mathbf{u})\cdot\mathbf{n})ds = \nu\nabla\phi\nabla\langle\mathbf{u}\rangle^i - \int_S \left(G\left(-\tilde{\Psi}\mathbf{I} + \nu\nabla\tilde{\mathbf{u}}\right)\cdot\mathbf{n}\right)ds, \tag{B.7}$$

where the term $-\nu\nabla\phi\nabla\langle\mathbf{u}\rangle^i$ on the r.h.s. is called "second Brinkman correction" (SBC) term. In a homogeneous porous medium, where the SBC term is zero, it has been shown (e.g., [7,13,32–34]) that the following closure can be used

$$\mathbf{F}_d = -\int_S \left(G\left(-\tilde{\Psi}\mathbf{I} + \nu\nabla\tilde{\mathbf{u}}\right)\cdot\mathbf{n}\right)ds = \nu\phi\langle\mathbf{u}\rangle\mathfrak{K}, \tag{B.8}$$

with $\mathfrak{K}$ the inverse of the permeability tensor. The SBC term is non zero in the transition zone across the interface between the fluid and homogeneous porous regions, where the porosity shows rapid changes, but the separation of scales $l_\mathcal{V} << L$, used to derive the SBC term, could not be valid, since the macroscopic flow variables undergo strong changes in a small distance.

Whitaker [32] pointed out there is no simple way for a closure in this thin transition region. In addition, when Goyeau et al. [14] studied the heterogeneous transition zone, obtained the jump conditions proposed in [34] omitting the SBC term, unlike Ochoa-Tapia and Whitaker [50] while using this term.

This derivation under the scale separation constraint $l_\mathcal{V} << L$ is provided here for comparative purposes, to highlight the theoretical limitations of standard macroscopic closures at the fluid-porous interface, which the present mesoscopic ODA model aims to overcome by using PSSs-informed spatial profiles.

Appendix C. Benefits of the new proposed principal anisotropic directions approach

In the present Appendix, we compare the results obtained in the framework of the mesoscopic averaged-scale approach, where the permeability profiles have been obtained according to the procedure described in the previous Section 3.2, assuming, the principal anisotropy directions aligned, in scenario 1, along the x and y directions, and, in scenario 2, along the tangential and orthogonal directions to the interface (see Section 3.2. The presented application is related to material M2 and $Re = 40$.

For scenario 1, where the rotation matrix $\mathbf{R} = \mathbf{I}$, assuming only the component of Eq. (8) along the $x-$direction, we get the map of the inverse of the permeability $\mathfrak{K}$ plotted in Fig. C.1, left, while Fig. C.1, right shows the map of $\mathfrak{K}$ computed according to the new approach in Section 3.2, applied for the simulations of scenario 2. In comparison with scenario 2, the higher values of $\mathfrak{K}$ for scenario 1 in the portions of the domain with approximately $\frac{3\pi}{4} \le \theta \le \frac{5\pi}{4}$ and $0 \le \theta \le \frac{\pi}{4}$ and $\frac{7\pi}{4} \le \theta \le 2\pi$ (with angle θ defined in Fig. 2, bottom right), mimic a higher resistance of the porous medium to the flow. This justifies the smaller (absolute) values of the flow velocity components and the higher pressure (absolute) values, especially close to the cylinder, as shown in Fig. C.2. The solution provided in scenario 2 fits much better the reference solution (averaged PSSs). In the presented results, the REV size used for the filtering operations is $l_\mathcal{V} = 2ul$. Similar results have been obtained using other porous materials, not shown for brevity.

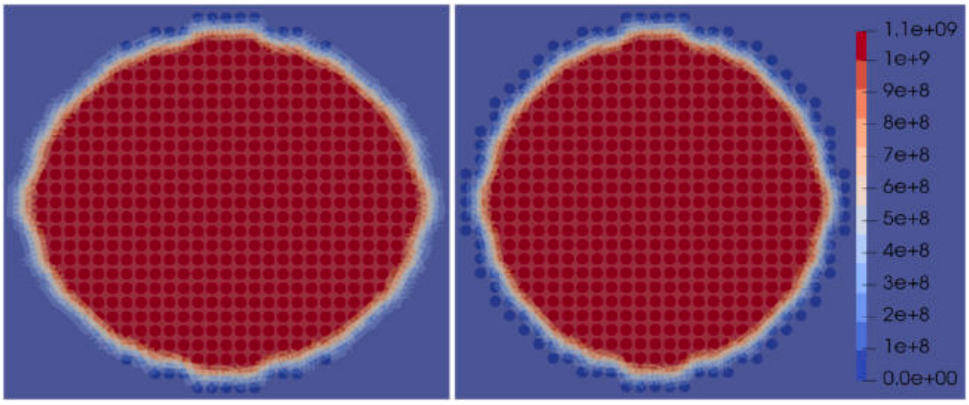

Fig. C.1. Inverse of the permeability $\mathfrak{K}$ in scenario 1 (left) and scenario 2 (right). Material M2, $Re = 40$.

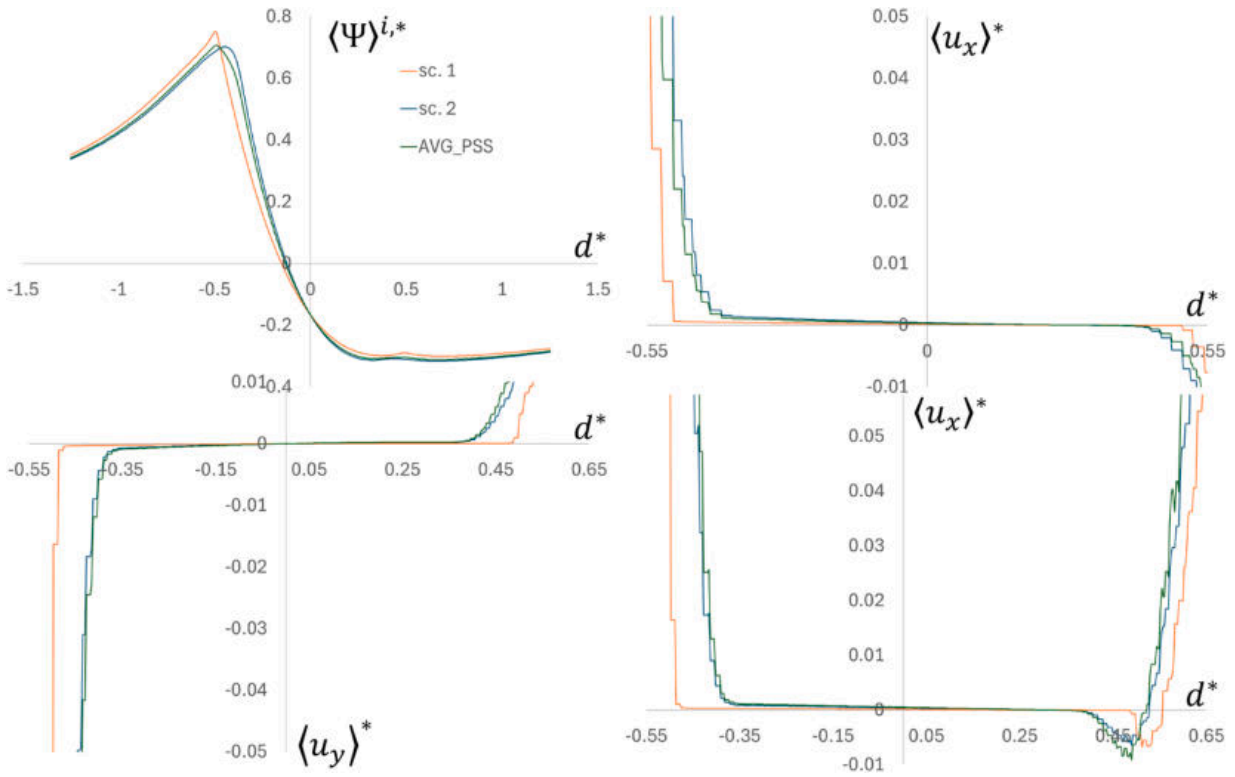

Fig. C.2. Computed (dimensionless) results. Top row. $\langle\Psi\rangle^{i,*}$ (left) and $\langle u_x\rangle^*$ (right) along the horizontal midline ($\theta = 0$). Bottom row. $\langle u_y\rangle^*$ (left) and $\langle u_x\rangle^*$ (right) along a $\theta = \frac{3\pi}{4}$ oriented line.

Appendix D. Comparison of the adopted solver in the penalized approach with literature data

In Fig. D.1 we compare the results provided by the solver in [42] in the "PODA" framework, with the outputs of the penalized solver proposed in [8]. Fig. D.1 shows the (dimensionless) wake geometrical parameters L_f, W_V, a, b obtained for a porous cylinder with a bulk Darcy number $Da_0 = 5 \cdot 10^{-06}$. The grid size close to the porous obstacle adopted in our simulations was $h^* = 0.012$, while in the literature study the authors used a much more refined grid ($h^* \simeq 0.0065$, see Table 1 and Fig. 3 in [8]). The plots in Fig. D.1 show very good agreement between the two solvers, and this also confirms the adequacy of the adopted grid size in our simulations.

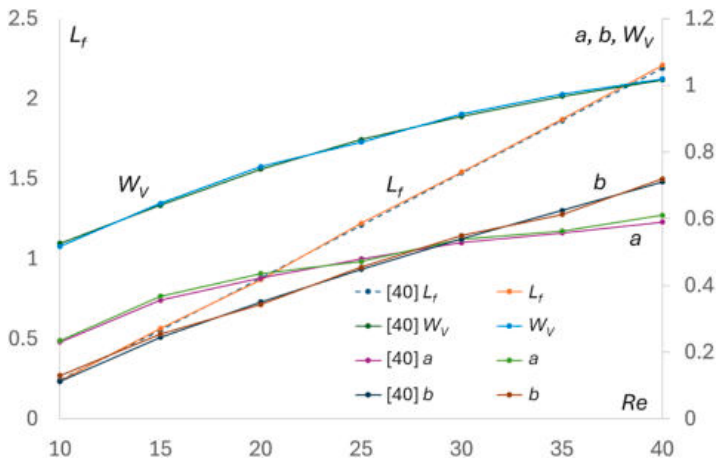

Fig. D.1. The geometrical wake parameters for a porous cylinder invested by a steady unconfined flow computed in the penalized framework. Comparison between the results provided by the solvers in [42] and [8].

References

[1] D. Gläser, R. Helmig, B. Flemisch, H. Class, A discrete fracture model for two-phase flow in fractured porous media, Adv. Water Resour. 110 (2017) 335–348. https://doi.org/10.1016/j.advwatres.2017.10.031

[2] K. Baber, B. Flemisch, R. Helmig, Modeling drop dynamics at the interface between free and porous-medium flow using the mortar method, Int. J. Heat Mass Transf. 99 (2016) 660–671. https://doi.org/10.1016/j.ijheatmasstransfer.2016.04.014

[3] C.-H. Bruneau, I. Mortazavi, Numerical modelling and passive flow control using porous media, Comput. Fluids 37 (5) (2008) 488–498. Special Issue Dedicated to Professor M.M. Hafez on the Occasion of his 60th Birthday, https://doi.org/10.1016/j.compfluid.2007.07.001

[4] M.L. Bars, M.G. Worster, Interfacial conditions between a pure fluid and a porous medium: implications for binary alloy solidification, J. Fluid Mech. 550 (2006) 149–173. https://api.semanticscholar.org/CorpusID:30548359.

[5] A.-R.A. Khaled, K. Vafai, The role of porous media in modeling flow and heat transfer in biological tissues, Int. J. Heat Mass Transf. 46 (26) (2003) 4989–5003. https://doi.org/10.1016/S0017-9310(03)00301-6

[6] T. Dbouk, D. Drikakis, Flow and plants, Phys. Fluids 36 (11) (2024) 110402. https://pubs.aip.org/aip/pof/article-pdf/doi/10.1063/5.0244727/20249641/110402_1_5.0244727.pdf, https://doi.org/10.1063/5.0244727.

[7] T. Tang, P. Yu, S. Yu, X. Shan, H. Chen, Connection between pore-scale and macroscopic flow characteristics of recirculating wake behind a porous cylinder, Phys. Fluids 32 (8) (2020) 083606. https://pubs.aip.org/aip/pof/article-pdf/doi/10.1063/5.0019262/16007766/083606_1_online.pdf, https://doi.org/10.1063/5.0019262

[8] P. Yu, Y. Zeng, T.S. Lee, X.B. Chen, H.T. Low, Steady flow around and through a permeable circular cylinder, Comput. Fluids 42 (1) (2011) 1–12. https://doi.org/10.1016/j.compfluid.2010.09.040

[9] S. Bhattacharyya, S. Dhinakaran, A. Khalili, Fluid motion around and through a porous cylinder, Chem. Eng. Sci. 61 (13) (2006) 4451–4461. The John Bridgwater Symposium: "Shaping the Future of Chemical Engineering", https://doi.org/10.1016/j.ces.2006.02.012

[10] S. Deo, P.K. Yadav, A. Tiwari, Slow viscous flow through a membrane built up from porous cylindrical particles with an impermeable core, Appl. Math. Model. 34 (5) (2010) 1329–1343. https://doi.org/10.1016/j.apm.2009.08.014

[11] G. Chen, C. Zou, H. Yang, S. Chen, P. Xie, A flow control strategy for a near-wall square cylinder using porous media: a direct numerical simulation study, Phys. Fluids 36 (2) (2024) 023108. https://pubs.aip.org/aip/pof/article-pdf/doi/10.1063/5.0188396/19616589/023108_1_5.0188396.pdf, https://doi.org/10.1063/5.0188396

[12] G.S. Beavers, D. Joseph, Boundary conditions at a naturally permeable wall, J. Fluid Mech. 30 (1967) 197–207. https://api.semanticscholar.org/CorpusID:123179601.

[13] M. Chandesris, D. Jamet, Boundary conditions at a planar fluid–porous interface for a Poiseuille flow, Int. J. Heat Mass Transf. 49 (13) (2006) 2137–2150. https://doi.org/10.1016/j.ijheatmasstransfer.2005.12.010

[14] B. Goyeau, D. Lhuillier, D. Gobin, M.G. Velarde, Momentum transport at a fluid–porous interface, Int. J. Heat Mass Transf. 46 (21) (2003) 4071–4081. https://doi.org/10.1016/S0017-9310(03)00241-2

[15] K. Vafai, C.L. Tien, Boundary and inertia effects on flow and heat transfer in porous media, Int. J. Heat Mass Transf. 24 (1981) 195–203. https://api.semanticscholar.org/CorpusID:36631576.

[16] C.-H. Bruneau, D. Lasseux, F.J. Valdés-Parada, Comparison between direct numerical simulations and effective models for fluid-porous flows using penalization, Meccanica 55 (5) (2020) 1061–1077. https://doi.org/10.1007/s11012-020-01149-7

[17] P. Angot, C.-H. Bruneau, P. Fabrie, A penalization method to take into account obstacles in incompressible viscous flows, Numer. Math. 81 (1999) 497–520. https://api.semanticscholar.org/CorpusID:28081622.

[18] S. Jamshed, R. Kharbanda, A.K. Dhiman, Study of flow through and around a pair of porous cylinders covering steady and unsteady regimes, Phys. Fluids 34 (10) (2022) 103601. https://pubs.aip.org/aip/pof/article-pdf/doi/10.1063/5.0113660/16578195/103601_1_online.pdf, https://doi.org/10.1063/5.0113660.

[19] H. Naito, K. Fukagata, Numerical simulation of flow around a circular cylinder having porous surface, Phys. Fluids 24 (11) (2012) 117102. https://pubs.aip.org/aip/pof/article-pdf/doi/10.1063/1.4767534/14130414/117102_1_online.pdf, https://doi.org/10.1063/1.4767534

[20] A. Parasyris, M. Discacciati, D.B. Das, Mathematical and numerical modelling of a circular cross-flow filtration module, Appl. Math. Model. 80 (2020) 84–98. https://doi.org/10.1016/j.apm.2019.11.016

[21] P. Yu, Y. Zeng, T.S. Lee, H.X. Bai, H.T. Low, Wake structure for flow past and through a porous square cylinder, Int. J. Heat Fluid Flow 31 (2) (2010) 141–153. https://doi.org/10.1016/j.ijheatfluidflow.2009.12.009

[22] Y. Amini, E. Izadpanah, M. Zeinali, A comprehensive study on the power-law fluid flow around and through a porous cylinder with different aspect ratios, Ocean Eng. 296 (2024) 117035. https://doi.org/10.1016/j.oceaneng.2024.117035

[23] W.P. Breugem, B.J. Boersma, R.E. Uittenbogaard, Direct numerical simulations of plane channel flow over a 3D Cartesian grid of cubes, in: Proc. Intl Conf. on Applications of Porous Media (ed. AH Reis & AF Miguel), 2004, pp. 27–34.

[24] T. Duman, U. Shavit, A solution of the laminar flow for a gradual transition between porous and fluid domains, Water Resour. Res. 46 (9) (2010). https://agupubs.onlinelibrary.wiley.com/doi/pdf/10.1029/2009WR008393, https://doi.org/10.1029/2009WR008393.

[25] W. Sadowski, F. di Mare, Investigation of the porous drag and permeability at the porous-fluid interface: influence of the filtering parameters on Darcy closure, Particuology 78 (2023) 122–135. https://doi.org/10.1016/j.partic.2022.09.010

[26] J.-L. Auriault, C. Boutin, C. Geindreau, Homogenization of Coupled Phenomena in Heterogeneous Media, ISTE, Wiley-ISTE, Hoboken, NJ, 2009. https://doi.org/10.1002/9780470612033

[27] F.J. Valdés-Parada, J. Alvarez-Ramírez, B. Goyeau, J.A. Ochoa-Tapia, Computation of jump coefficients for momentum transfer between a porous medium and a fluid using a closed generalized transfer equation, Transp. Porous Media 78 (3) (2009) 439–457. https://doi.org/10.1007/s11242-009-9370-9

[28] R. Hernandez-Rodriguez, P. Angot, B. Goyeau, J.A. Ochoa-Tapia, Momentum transport in the free fluid-porous medium transition layer: one-domain approach, Chem. Eng. Sci. 248 (2022) 117111. https://doi.org/10.1016/j.ces.2021.117111

[29] F.J. Valdès-Parada, D. Lasseux, A novel one-domain approach for modeling flow in a fluid-porous system including inertia and slip effects, Phys. Fluids 33 (2) (2021) 022106. https://pubs.aip.org/aip/pof/article-pdf/doi/10.1063/5.0036812/13788659/022106_1_online.pdf, https://doi.org/10.1063/5.0036812

[30] F.J. Valdès-Parada, D. Lasseux, Flow near porous media boundaries including inertia and slip: a one-domain approach, Phys. Fluids 33 (7) (2021) 073612. https://pubs.aip.org/aip/pof/article-pdf/doi/10.1063/5.0056345/13831037/073612_1_online.pdf, https://doi.org/10.1063/5.0056345.

[31] W.G. Gray, A derivation of the equations for multi-phase transport, Chem. Eng. Sci. 30 (2) (1975) 229–233. https://doi.org/10.1016/0009-2509(75)80010-8

[32] S. Whitaker, Flow in porous media I: a theoretical derivation of Darcy's law, Transp. Porous Media 1 (1986). https://www.osti.gov/biblio/6416113. https://doi.org/10.1007/BF01036523

[33] M. Quintard, S. Whitaker, Transport in ordered and disordered porous media II: generalized volume averaging, Transp. Porous Media 14 (1994) 179–206. https://api.semanticscholar.org/CorpusID:121377010.

[34] J.A. Ochoa-Tapia, S. Whitaker, Momentum transfer at the boundary between a porous medium and a homogeneous fluid–I. Theoretical development, Int. J. Heat Mass Transf. 38 (14) (1995) 2635–2646. https://doi.org/10.1016/0017-9310(94)00346-W

[35] W. Breugem, The Influence of Wall Permeability on Laminar and Turbulent Flows: Theory and Simulations, Ph.D. thesis, Doctoral. TU Delft, Delft, 2004.

[36] N. Tilton, L. Cortelezzi, Linear stability analysis of pressure-driven flows in channels with porous walls, J. Fluid Mech. 604 (2008) 411–445. https://api.semanticscholar.org/CorpusID:121178892.

[37] W.P. Breugem, B.J. Boersma, R.E. Uittenbogaard, The influence of wall permeability on turbulent channel flow, J. Fluid Mech. 562 (2006) 35–72. https://doi.org/10.1017/S0022112006000887

[38] S. Whitaker, The Forchheimer equation: a theoretical development, Transp. Porous Media 25 (1) (1996) 27–61. https://doi.org/10.1007/BF00141261

[39] M. Chandesris, D. Jamet, Derivation of jump conditions for the turbulence $k-\epsilon$ model at a fluid/porous interface, Int. J. Heat Fluid Flow 30 (2) (2009) 306–318. https://doi.org/10.1016/j.ijheatfluidflow.2009.01.008

[40] C. Aricò, M. Sinagra, C. Picone, T. Tucciarelli, MAST-RT0 Solution of the incompressible Navier-Stokes equations in 3D complex domains, Eng. Appl. Comput. Fluid Mech. 15 (1) (2021) 53–93. https://doi.org/10.1080/19942060.2020.1860830
[41] C. Aricò, M. Sinagra, Z. Driss, T. Tucciarelli, A new solver for incompressible non-isothermal flows in natural and mixed convection over unstructured grids, Appl. Math. Model. 103 (2022) 445–474. https://doi.org/10.1016/j.apm.2021.10.042
[42] C. Aricò, R. Helmig, D. Puleo, M. Schneider, A new numerical mesoscopic scale one-domain approach solver for free fluid/porous medium interaction, Comput. Methods Appl. Mech. Eng. 419 (2024) 116655. https://doi.org/10.1016/j.cma.2023.116655
[43] J. Bear, Dynamics of Fluids in Porous Media, American Elsevier Publishing Company, New York, 1972.
[44] A.S. Sangani, A. Acrivos, Slow flow past periodic arrays of cylinders with application to heat transfer, Int. J. Multiphase Flow 8 (3) (1982) 193–206. https://doi.org/10.1016/0301-9322(82)90029-5
[45] C.Y. Wang, Stokes flow through a rectangular array of circular cylinders, Fluid Dyn. Res. 29 (2) (2001) 65. https://doi.org/10.1016/S0169-5983(01)00013-2
[46] M. Coutanceau, R. Bouard, Experimental determination of the main features of the viscous flow in the wake of a circular cylinder in uniform translation. Part 1. Steady flow, J. Fluid Mech. 79 ER (2) (1977) 231–256. https://doi.org/10.1017/S0022112077000135
[47] B. Fornberg, A numerical study of steady viscous flow past a circular cylinder, J. Fluid Mech. 98 (4) (1980) 819–855. https://doi.org/10.1017/S0022112080000419
[48] S.C.R. Dennis, G.-Z. Chang, Numerical solutions for steady flow past a circular cylinder at Reynolds numbers up to 100, J. Fluid Mech. 42 (3) (1970) 471–489. https://doi.org/10.1017/S0022112070001428
[49] S. Sen, S. Mittal, G. Biswas, Steady separated flow past a circular cylinder at low Reynolds numbers, J. Fluid Mech. 620 ER (2009) 89–119. https://doi.org/10.1017/S0022112008004904
[50] J.A. Ochoa-Tapia, S. Whitaker, Momentum transfer at the boundary between a porous medium and a homogeneous fluid–II. Comparison with experiment, Int. J. Heat Mass Transf. 38 (14) (1995) 2647–2655. https://doi.org/10.1016/0017-9310(94)00347-X